Draft version July 14, 2025
Typeset using LaTeX twocolumn style in AASTeX631

MOSDEF-3D: Keck/OSIRIS Maps of the Ionized ISM in z ∼ 2 Galaxies

Natalie Lam,[1] Alice E. Shapley,[1] Ryan L. Sanders,[2] Tuan Do,[1] Tucker Jones,[3] Alison Coil,[4] Mariska Kriek,[5] Bahram Mobasher,[6] Naveen A. Reddy,[6] Brian Siana,[6] and Leonardo Clarke[1]

[1]Department of Physics & Astronomy, University of California, Los Angeles, 430 Portola Plaza, Los Angeles, CA 90095, USA
[2]Department of Physics and Astronomy, University of Kentucky, 505 Rose Street, Lexington, KY 40506, USA
[3]Department of Physics and Astronomy, University of California Davis, 1 Shields Avenue, Davis, CA 95616, USA
[4]Department of Astronomy & Astrophysics, University of California, San Diego, La Jolla, CA 92092, USA
[5]Leiden Observatory, Leiden University, NL-2300 RA Leiden, Netherlands
[6]Department of Physics & Astronomy, University of California, Riverside, 900 University Avenue, Riverside, CA 92521, USA

ABSTRACT

We present spatially-resolved rest-frame optical emission line maps of four galaxies at $z \sim 2$ observed with Keck/OSIRIS to study the physical conditions of the ISM at Cosmic Noon. Our analysis of strong emission line ratios in these galaxies reveals an offset from the local star-forming locus on the BPT diagram, but agrees with other star-forming galaxies at similar redshifts. Despite the offset towards higher [O III]λ5008/Hβ and [N II]λ6585/Hα, these strong-line ratios remain consistent with or below the maximum starburst threshold even in the inner ~ 1 kpc region of the galaxies, providing no compelling evidence for central AGN activity. The galaxies also exhibit flat radial gas-phase metallicity gradients, consistent with previous studies of $z \sim 2$ galaxies and suggesting efficient radial mixing possibly driven by strong outflows from intense star formation. Overall, our results reveal the highly star-forming nature of these galaxies, with the potential to launch outflows that flatten metallicity gradients through significant radial gas mixing. Future observations with JWST/NIRSpec are crucial to detect fainter emission lines at higher spatial resolution to further constrain the physical processes and ionization mechanisms that shape the ISM during Cosmic Noon.

Keywords: High-redshift galaxies(734) — Emission line galaxies(459) — Interstellar medium(847) — Galaxy evolution(594)

1. INTRODUCTION

During the peak of cosmic star formation activity, commonly referred to as "Cosmic Noon" (redshift $z \sim 2$), star-formation and gas accretion rates were significantly higher than in the local universe (e.g., Madau & Dickinson 2014; Tacconi et al. 2020). The physical conditions of the interstellar medium (ISM) in galaxies at this epoch differ from those in the present-day universe, with notable variations in chemical composition, ionization states, and gas dynamics. Intense star formation in these systems can drive large-scale gas flows, one of the key feedback mechanisms that regulates galaxy evolution (e.g., Förster Schreiber et al. 2018). The rest-frame optical spectrum serves as a valuable probe of the ISM. It contains recombination lines such as Hα and Hβ and collisionally excited lines, including [O III], [N II], and [S II]. These features trace physical properties of the ionized ISM including dust content, ionization conditions, and gas-phase metallicity.

A key diagnostic for understanding the ionization properties of galaxies is the Baldwin-Phillips-Terlevich (BPT) diagram (Baldwin et al. 1981), which empirically separates star-forming galaxies from those hosting active galactic nuclei (AGN) based on strong emission-line ratios. When applied to integrated galaxy spectra, the BPT diagram has been widely used to classify ionization sources. However, high-redshift star-forming galaxies exhibit a systematic offset from the local star-forming sequence, where [O III]λ5008/Hβ and [N II]λ6585/Hα ratios are elevated (e.g., Steidel et al. 2014; Strom et al. 2017; Runco et al. 2021; Shapley et al. 2025). This systematic offset can push star-forming galaxies towards regions typically populated by AGN with low mass or high specific star formation rate host galaxies (Coil et al. 2015). The physical origin of the offset in the star-forming sequence was previously under debate, with proposed explanations including higher nitrogen-to-oxygen (N/O) ratios at fixed oxygen abundance (e.g., Masters

et al. 2014), harder ionizing spectra from massive stars (e.g., Shapley et al. 2015; Sanders et al. 2023), and higher ionization parameters (e.g., Bian et al. 2020). However, a preponderance of recent data now points toward harder ionizing spectra at fixed metallicity as the primary cause (e.g., Steidel et al. 2016; Cullen et al. 2021; Shapley et al. 2025)

Significant progress has been made in characterizing high-redshift galaxies through decades of spectroscopic studies, providing key insights into their physical properties and evolution. Near-IR spectrographs on ground-based 8–10 m telescopes and the Hubble Space Telescope (HST) have enabled the spectroscopic study of galaxies up to $z \sim 3$ (e.g., Steidel et al. 2014; Shapley et al. 2015; Momcheva et al. 2016; Kashino et al. 2017; Förster Schreiber et al. 2019). Recently, the redshift frontier has been extended significantly further with the advent of JWST, enabling rest-frame optical spectroscopy out to $z \sim 11 - 14$ and beyond (e.g., Carniani et al. 2024; Napolitano et al. 2025). This extensive sample of galaxies across a wide range of redshifts provides statistical leverage on global properties such as metallicity, ionization conditions, and AGN activity. However, the majority of these studies rely on integrated spectra, where emission from different spatial regions is blended within a single aperture (but see, e.g., Jones et al. (2024)). This blending obscures the contribution of distinct ionization sources and spatially varying physical conditions, limiting the ability to fully disentangle the processes driving galaxy evolution.

Integral field unit (IFU) spectroscopy thus provides a crucial advantage by resolving spatial variations in emission-line ratios, allowing for a more nuanced interpretation of ionization conditions. By resolving spatial variations in line ratios and gas kinematics, IFU data can alleviate degeneracies and separate distinct ionization sources (e.g. star-forming regions, AGN, shocks) and kinematic components that may be mixed in integrated spectra (e.g., Förster Schreiber et al. 2018; Übler et al. 2024). Spatially resolved BPT diagnostics enable the identification of weak or obscured AGN that may influence central emission-line ratios in predominantly star-forming galaxies (e.g., Wright et al. 2010), as well as the mapping of ionization structure within galaxies to constrain the underlying physical mechanisms (e.g., Jones et al. 2024; Parlanti et al. 2025).

Another key spatial diagnostic is the radial trend in gas-phase metallicity, often traced by strong-line ratios such as the [N II]λ6585/Hα flux ratio. In the local universe, star-forming disk galaxies exhibit a mild negative metallicity gradient (~ -0.05 dex kpc^{-1}), consistent with inside-out galaxy growth (e.g., Rupke et al. 2010; Sánchez, S. F. et al. 2014). At high redshift, however, metallicity gradients are observed to be largely flat (e.g., Curti et al. 2020; Wang et al. 2020; Ju et al. 2025), suggestive of efficient radial mixing due to strong feedback processes (e.g., Gibson et al. 2013; Ma et al. 2017). A subset of high-redshift galaxies show either negative (Jones et al. 2010, 2013) or even inverted gradients, the latter potentially indicative of metal-poor gas accretion (e.g., Wang et al. 2019; Li et al. 2022). On the theoretical side, cosmological simulations with smooth stellar feedback produce strongly negative metallicity gradients at high-redshifts (e.g., Garcia et al. 2025), which is in contention with the flat gradients from observations. The large scatter in observed metallicity gradients and the mismatch with simulations point to a diverse range of physical mechanisms shaping galaxy evolution and ISM physical conditions during this epoch.

In this study, we present Keck/OSIRIS IFU observations of four galaxies at $z \sim 2$, leveraging both high spectral ($R \sim 3600$) and spatial resolution to investigate spatial variations in strong emission-line ratios. The largest sample of spatially resolved high-redshift galaxies to date comes from Wang et al. (2020), based on low-resolution HST grism spectroscopy ($R \sim 100$). Other ground-based IFU studies have also contributed to increase the sample size (e.g., Förster Schreiber et al. 2019; Curti et al. 2020), though observations are seeing-limited or are restricted to lensed galaxies. Our observations thus build on this foundation by utilizing the higher spectral resolution of OSIRIS to enable detailed multi-component emission-line fitting, as well as adaptive optics (AO) to achieve higher spatial resolution. Our work complements existing studies by providing new constraints on ionization conditions, AGN activity, and metallicity distributions within these galaxies, ultimately broadening our understanding of stellar feedback, outflows, and galaxy evolution.

The structure of this paper is as follows: in Section 2, we describe the observations and data reduction; in Section 3, we outline our methodology for spatial binning and emission-line fitting; in Section 4, we present results on BPT diagnostics and radial [N II]λ6585/Hα gradients; and in Section 5, we discuss the implications of our findings in the context of galaxy evolution.

Throughout this paper, we assume a ΛCDM cosmology with $H_0 = 70$ km s^{-1} Mpc^{-1}, $\Omega_m = 0.3$, and $\Omega_\Lambda = 0.7$.

2. OBSERVATIONS & DATA REDUCTION

2.1. *Targets & observations*

The four galaxies analyzed in this study are drawn from the MOSFIRE Deep Evolution Field (MOSDEF)

survey (Kriek et al. 2015), which provides rest-frame optical spectroscopy for a sample of $\sim$ 1500 galaxies spanning a redshift range of $1.4 < z < 3.8$. These particular targets are among the brightest emission-line galaxies within the survey, and thus were selected for OSIRIS follow-up with the goal of detecting key diagnostic emission lines such as Hβ, [O III]$\lambda\lambda 4960, 5008$, H$\alpha$, and [N II]$\lambda\lambda 6548, 6585$ with high signal-to-noise. At the redshifts of these galaxies ($z \sim 2$), these emission lines fall within the H and K bands.

Furthermore, three out of the four galaxies displayed signatures of gas flow from their MOSDEF spectra, where COSMOS 19985 and COSMOS 20062 have clearly-detected broad kinematic components in the strong emission lines listed above (Leung et al. 2017), and GOODS-S 40768 shows a redshifted kinematic component indicative of gas infall (Weldon et al. 2023).

A key consideration in target selection was the integrated flux of Hα, which is typically the brightest rest-optical emission line within the MOSDEF samples. Sufficiently bright integrated Hα flux ($\geq 1.5 \times 10^{-16}$ erg s^{-1} cm^{-2}) is needed for reliable detection of fainter emission lines such as [N II]λ6585 and Hβ given the typical line ratios observed in $z \sim 2$ star-forming galaxies. Additionally, each galaxy was required to have a tip-tilt star with an R-band magnitude of $R = 17$ or brighter within a 60" radius, enabling the use of adaptive optics (AO) correction to achieve $\sim$ 0.1" resolution.

Each of these galaxies also has corresponding rest-frame UV spectroscopic observations obtained with Keck/LRIS, providing complementary constraints on their ionizing radiation fields and extended gas flow kinematics (Topping et al. 2020; Weldon et al. 2022).

Observations were conducted using the OH-Suppressing Infra-Red Imaging Spectrograph (OSIRIS) (Larkin et al. 2006) on the Keck I telescope, which is an integral field unit (IFU) operating in the near-infrared (NIR). OSIRIS, when used with the Keck adaptive optics system, enables spatially resolved spectroscopy at resolutions of $\sim$ 0.1", which corresponds to $\sim$ 1 kpc at $z \sim 2$. This high angular resolution is critical for studying the spatial variations in emission-line properties across each galaxy.

The four OSIRIS target galaxies were observed on five different nights spanning May 2017, January 2018, and June 2018. Each galaxy was observed in both the H narrow band (Hn2 or Hn3) and K broad band (Kbb) using a lenslet plate scale of 0.05" and with Laser Guide Star (LGS) AO. Each individual frame was exposed for 900 seconds to give a total exposure time that ranged from 5400–12600 seconds in the H bands and 5400–10800 seconds in the K bands. A dither of 1.6" in the long axis of the FOV was applied between exposures to enable sky subtraction. Information about the observations is listed in Table 1.

2.2. *Data reduction*

The observations were reduced using the OSIRIS Data Reduction Pipeline (Lyke et al. 2017; Lockhart et al. 2019), with several modifications to the standard reduction procedure due to the absence of a dedicated sky frame.

Initially, a bad pixel mask was applied to correct for detector defects, followed by the subtraction of a master dark that was generated from median-combining several dark frames observed at the start of the night. The pipeline then applied previously-measured lenslet spectral-PSF maps to construct the datacube using a process similar to Lucy-Richardson deconvolution.

Sky subtraction was achieved by using the pipeline's scaled sky subtraction procedure, which measures the flux of the brightest OH emission lines to determine the scaling of the corresponding families of lines for sky-line subtraction. In lieu of a dedicated sky frame, we applied the procedure on pairs of dithered images by subtracting each from the other. The resulting frames were then mosaicked using a sigma clipping algorithm.

To estimate the Point Spread Function (PSF) of the data, the same process was applied to the observations of the tip-tilt stars associated with each galaxy. We fitted a symmetric 2D-Gaussian to the flux map obtained by summing up the flux within each spatial pixel (spaxel) and defined the PSF of the observations as the Full Width at Half Maximum (FWHM) of the 2D-Gaussian model. These values are quoted in Table 1, with an average of 0.123" in the H bands and 0.120" in the K band.

During the reduction process, it became evident that the error spectra generated by the pipeline were elevated relative to the noise estimated empirically in parts of the spectra between strong OH emission lines. To address this inconsistency and scale down the pipeline error spectra, we first defined wavelength windows in regions that lacked significant OH line emission, with observed widths of $\sim$ 30 Å in the H band and $\sim$ 50 Å in the K band. We then calculated the ratio between the 1σ standard deviation of the flux and the median of the pipeline error spectrum within these windows for each spaxel, taking the median ratio across the wavelength windows in each spaxel to obtain a map of error-scaling factors. The median value of this error-scaling factor

Table 1. Observation Details

ID	R.A. (J2000)	Dec. (J2000)	z	Date (MM/DD/YY)	Filter	t_{exp} (s)	PSF (")	H_{160} (AB mag)
COSMOS 19985	10:00:14.484	+02:22:57.98	2.1882	01/02/18	Hn2	5400	0.130	21.87
				01/02/18	Kbb	9000	0.123	
COSMOS 20062	10:00:16.436	+02:23:00.79	2.1857	01/03/18	Hn2	7200	0.140	22.10
				01/03/18	Kbb	5400	0.142	
AEGIS 3668	14:19:28.839	+52:46:24.62	2.1877	05/17/17	Hn2	7200	0.114	22.35
				05/18/17, 06/05/18	Kbb	10800	0.117	
GOODS-S 40768	03:32:09.797	-27:43:08.65	2.3035	01/02/18	Hn3	12600	0.109	22.04
				01/03/18	Kbb	5400	0.097	

map was then applied uniformly to rescale the pipeline error spectrum across all spaxels.

Additionally, the OH emission lines in the raw science frames appeared to be offset from their expected wavelengths based on the known wavelengths of near-IR OH sky lines. We corrected for this offset by performing centroiding on the OH emission lines in a dark-subtracted, non-sky-subtracted science data cube, calculating the mean offset per spaxel, and applying mean value of all these offsets to shift the wavelength calibration of the final reduced data. The averages of these offsets are -2.18 ± 0.04 Å and -3.29 ± 0.05 Å in the H- and K-bands for the 2018 observations (i.e. COSMOS 19985, COSMOS 20062, and GOODS-S 40768), and ~ 0.32 Å and ~ 0.53 Å in the H- and K-bands for the 2017 observations (i.e. AEGIS 3668).

3. ANALYSIS

3.1. *Spatial binning*

To obtain robust emission-line maps that are based on line ratios spanning the H and K bands, it is essential to align the data cubes to ensure that we are comparing the same physical regions of the galaxy across both bands. To achieve this alignment, we first created flux maps for a 10 Å window centered around the strongest emission lines in each band ([O III]λ5008 for H band and Hα for K band). These maps were normalized to the brightest pixel near the galaxy's center. To align the bands, we computed the squared residuals between the flux maps, shifting the H band flux map relative to the K band flux map iteratively on integer spaxel increments and identifying the configuration that minimized the residuals. Lastly, we cropped the data in both bands to the same size, which is typically limited by the FOV of the K-band data.

We applied two types of spatial binning methods for our subsequent analysis. First, we performed a coarser radial or circular aperture binning on both H and K bands for the BPT diagram analysis. Second, we applied a finer Voronoi binning based on the higher S/N data in the K band to enable a more detailed examination of the [N II]λ6585/Hα ratio. These binning strategies are described in detail in the following sections.

3.1.1. *Radial and clump binning*

For galaxies COSMOS 19985, COSMOS 20062 and AEGIS 3665, radial binning was employed to investigate spatial variations in emission line properties with increasing distance from the center of the objects. A 2D Gaussian was fit to the higher-S/N K-band flux map of each galaxy to parameterize the elliptical morphology, with key parameters such as semi-major and semi-minor axes containing the central 68.3% of the flux (i.e., one spatial standard deviation), orientation, and centroid. Using this parameterization, we extracted regions encompassing up to 99.7% of the flux (i.e., 3 spatial standard deviations) and generated a mask to isolate the galaxy in both bands. Radial bins were then constructed, with a central bin encompassing 1 spatial-σ of the flux and additional annuli encompassing 2 spatial-σ and 3 spatial-σ flux levels. These bins are named R1σ, R2σ, and R3σ respectively. The radial bin map for each galaxy is given in the bottom-left panel of Figs. 1-3.

Due to the unusual morphology of GOODS-S 40768 consisting of three distinct clumps, instead of radial binning, we defined three circular apertures centered on regions exhibiting similar kinematics. The center, East, and West bins shown in Figs. 4 have radii 0.175", 0.125", and 0.15" respectively. Another clump with higher Hα surface brightness is identified to the northwest of the center of COSMOS 20062, so an additional circular aperture of radius 0.1" was defined to isolate this distinct clump.

For each bin, the mean spectrum was calculated by averaging the flux across all spaxels within the bin. The error spectrum was summed in quadrature across the

spaxels and divided by the square root of the number of spaxels in the bin, yielding a representative uncertainty for the mean spectrum.

3.1.2. *Voronoi binning*

In the case of joint analyses of H- and K-band data, the spatial resolution of the radial bins described above is limited by the lower S/N in the H band. Since the examination of radial variations in [N II]λ6585/Hα ratios only depends on K-band data, we adopt finer bins using Voronoi binning for this higher S/N data to enhance the spatial resolution of this analysis. Voronoi binning was applied using the Python package `vorbin` (Cappellari & Copin 2003). This method takes a S/N map and groups spaxels together to reach a target S/N threshold while striving to make the bins as round as possible, thereby preserving maximum spatial resolution. For this analysis, the binning was performed using the Hα flux map and the 3 spatial-σ elliptical mask described above. The associated error map was constructed as the 1σ standard deviation in flux values from neighboring continuum wavelength regions. Spaxels with S/N < 1 were excluded from further analysis.

Voronoi binning was applied to COSMOS 19985, COSMOS 20062, and AEGIS 3668. The object GOODS-S 40768 was excluded from this method since the clump bins in Section 3.1.1 already describe the spatial variations well and low S/N prevents additional bins from being created. The target S/N threshold for the two COSMOS objects were set such that the [N II]λ6585 emission line reaches a minimum of $S/N \sim 3$ in every bin. Due to the low [N II]λ6585 flux in AEGIS 3668, we imposed a less stringent limit on its [N II]λ6585 S/N. Instead, the target S/N of Hα for Voronoi binning of AEGIS 3668 was set to be comparable to that of the two COSMOS objects, which had target $S/N \sim 25$.

Figures 1– 4 show the maps of the spatial binning strategies as described above.

3.2. *Spectral analysis*

3.2.1. *Emission line fitting*

Emission line fitting was performed using the Python package `lmfit` to model the spectral features of each galaxy. We fit the [N II]$\lambda\lambda$6548, 6585+Hα and [O III]$\lambda\lambda$4960, 5008+Hβ emission lines simultaneously within their respective groups using Gaussian profiles parameterized by flux, Doppler shift, and broadening, each corresponding to the amplitude, center, and width of a Gaussian.

For each group, we tied the Doppler shift and broadening width of the weaker lines to those of the strongest line in the group – Hα for the [N II]$\lambda\lambda$6548, 6585+Hα group and [O III]λ5008 for the [O III]$\lambda\lambda$4960, 5008+Hβ group. The flux ratios of the [N II]$\lambda\lambda$6548, 6585 doublet and the [O III]$\lambda\lambda$4960, 5008 doublet were fixed to their theoretical values of 2.94 and 2.98, respectively.

After enforcing the above relationships, we ended up with four key fitting parameters for each group:

1. Center of the strongest line ([O III]λ5008 or Hα)
2. Broadening width of the strongest line
3. Flux of the hydrogen recombination line (Hα or Hβ)
4. Flux of the stronger metal line ([N II]λ6585 or [O III]λ5008)

We applied two types of fits to each group of emission lines. The one-component model used a single Gaussian per emission line, resulting in a total of three Gaussians per group and four fitting parameters. In contrast, the two-component model had two Gaussians per emission line: a narrow component (C1) representing systemic gas and a broad component (C2) representing gas flows. The line centers for C1 and C2 were allowed to differ. This approach resulted in a total of six Gaussians per group and eight fitting parameters. In the two-component model, the narrow component (C1) was constrained to have a narrower width, tracing the local velocity dispersion in the ionized ISM, while the broad component (C2) captured possible signatures of gas flow. We treat the fitted Gaussians in the one-component model as a narrow component.

Additional models were also employed in response to poor fits to certain spectra from visual inspection. Details about these more complex models and the spectrum that was best fit by one of such models will be discussed in Section 3.2.3.

To ensure physically reasonable fits, we imposed limits on the velocity shifts and broadening parameters. The bounds were chosen to be loose enough to prevent the fit from adopting the bound values but strict enough to be physically reasonable. For one-component fits, we allowed a maximum velocity shift of ± 500 km s^{-1} and a maximum FWHM of 2000 km s^{-1}. In two-component fits, we introduced a more restrictive narrow component with velocity shift limit of ± 100 km s^{-1} and maximum FWHM of 1000 km s^{-1}. Additionally, the minimum FWHM was set based on the spectral resolution of $R \sim 3600$, and flux values were restricted to be non-negative.

Fitting errors were estimated using the square root of the diagonal terms of the covariance matrix. To avoid overfitting with the two-component model, we used the Bayesian Information Criterion (BIC; Kass & Raftery

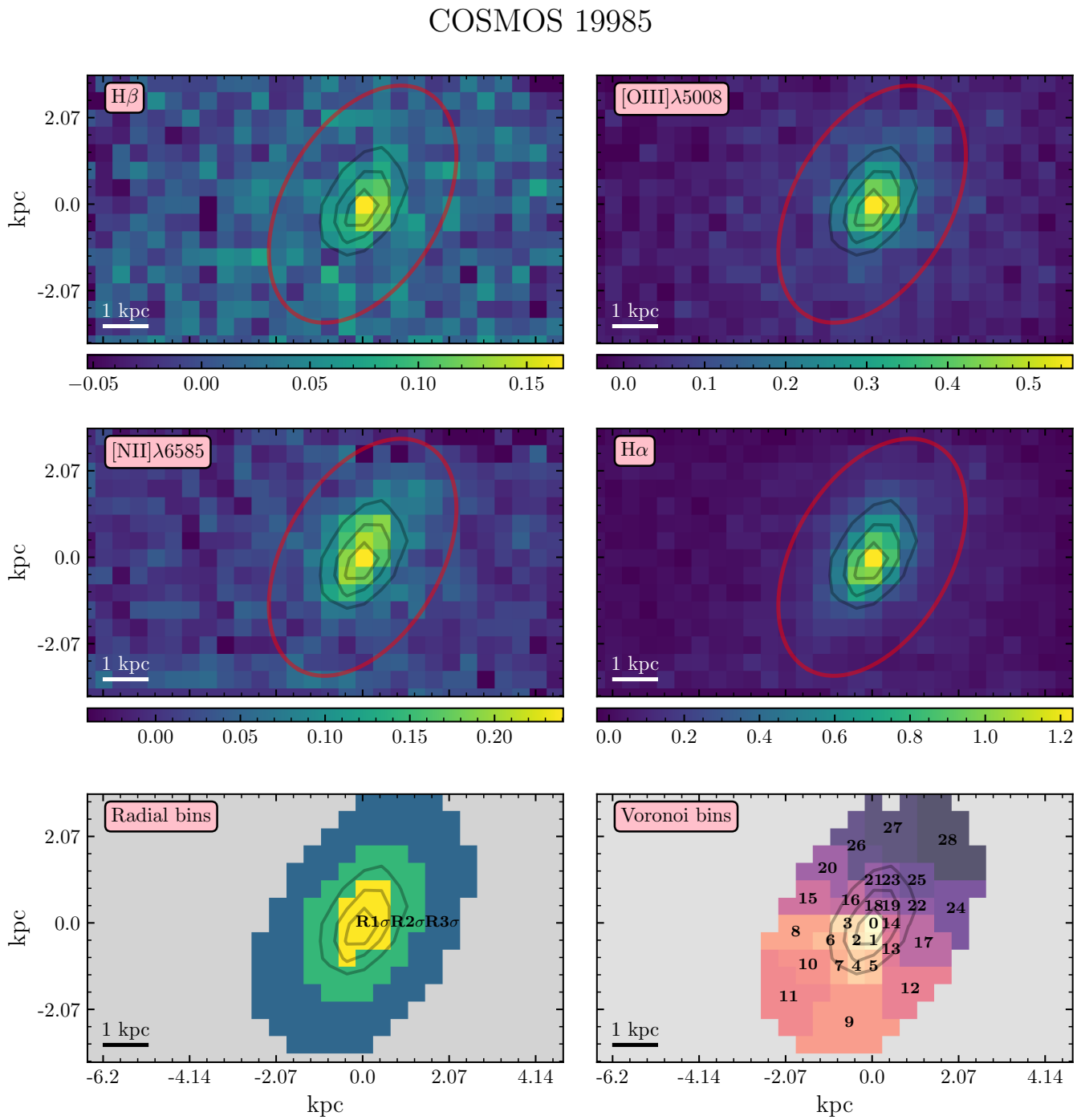

Figure 1. Emission line flux maps and spatial binning maps for COSMOS 19985. The upper four maps represent the summed flux in a rest-frame 10 Å window centered around Hβ, [O III]λ5008, [N II]λ6585, and Hα with arbitrary flux units. Gray contours that trace the Hα flux are overlaid on top of each map for reference. The red ellipses mark the 3-σ flux-level threshold of the galaxy based on a 2D-Gaussian model. The bottom left map shows the radial bins generated from the 1-σ, 2-σ, and 3-σ flux-level thresholds, while the bottom right map shows the Voronoi bins. Bin colors are added for clarity.

1995) to assess model preference. For the more complex two-component model to be favored, we required its BIC value to be at least 6 lower than that of the one-component model; otherwise, the one-component model was selected.

For the integrated OSIRIS and radially-binned spectra, we further cross-checked the fitting between the H

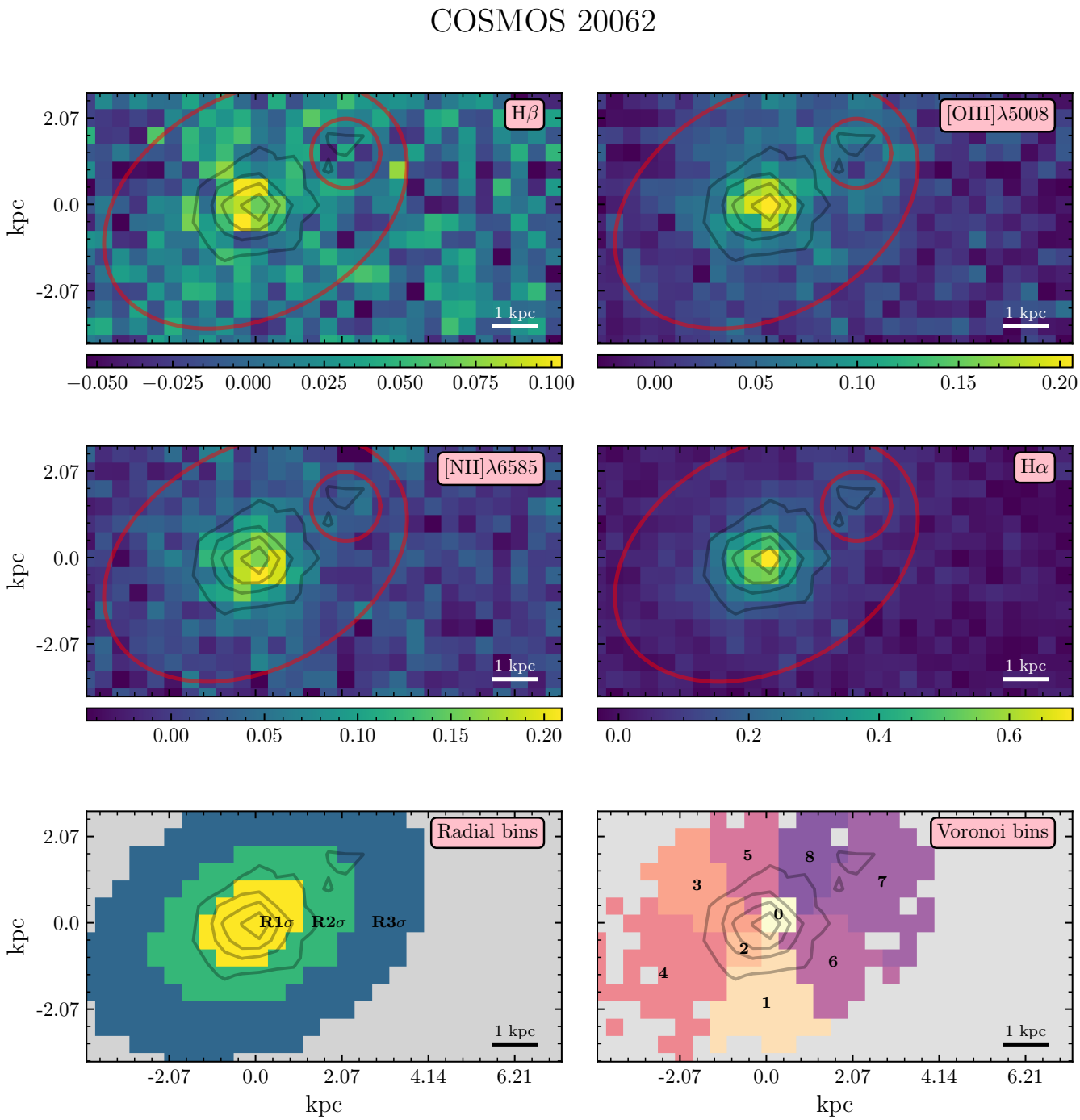

Figure 2. Emission line flux maps and spatial binning maps for COSMOS 20062, as in Fig. 1. The additional small red circle denotes the clump bin with radius.

and K bands. In cases where the [N II]$\lambda\lambda$6548, 6585+Hα and [O III]$\lambda\lambda$4960, 5008+Hβ groups disagreed on the preferred component fit (i.e., one- vs. two-component), refitting was performed based on the preferred component fit of the higher S/N data (typically the K band with [N II]$\lambda\lambda$6548, 6585+Hα). The S/N was calculated as the ratio of the flux to the fitting error of the strongest line in the group. During refitting, the velocity shift and broadening width were fixed to the fitted values from the higher S/N data, while only the fluxes were allowed to vary in the lower S/N data (typically the H band with [O III]$\lambda\lambda$4960, 5008+Hβ). Fig. 5 shows a schematic of the above fitting routine.

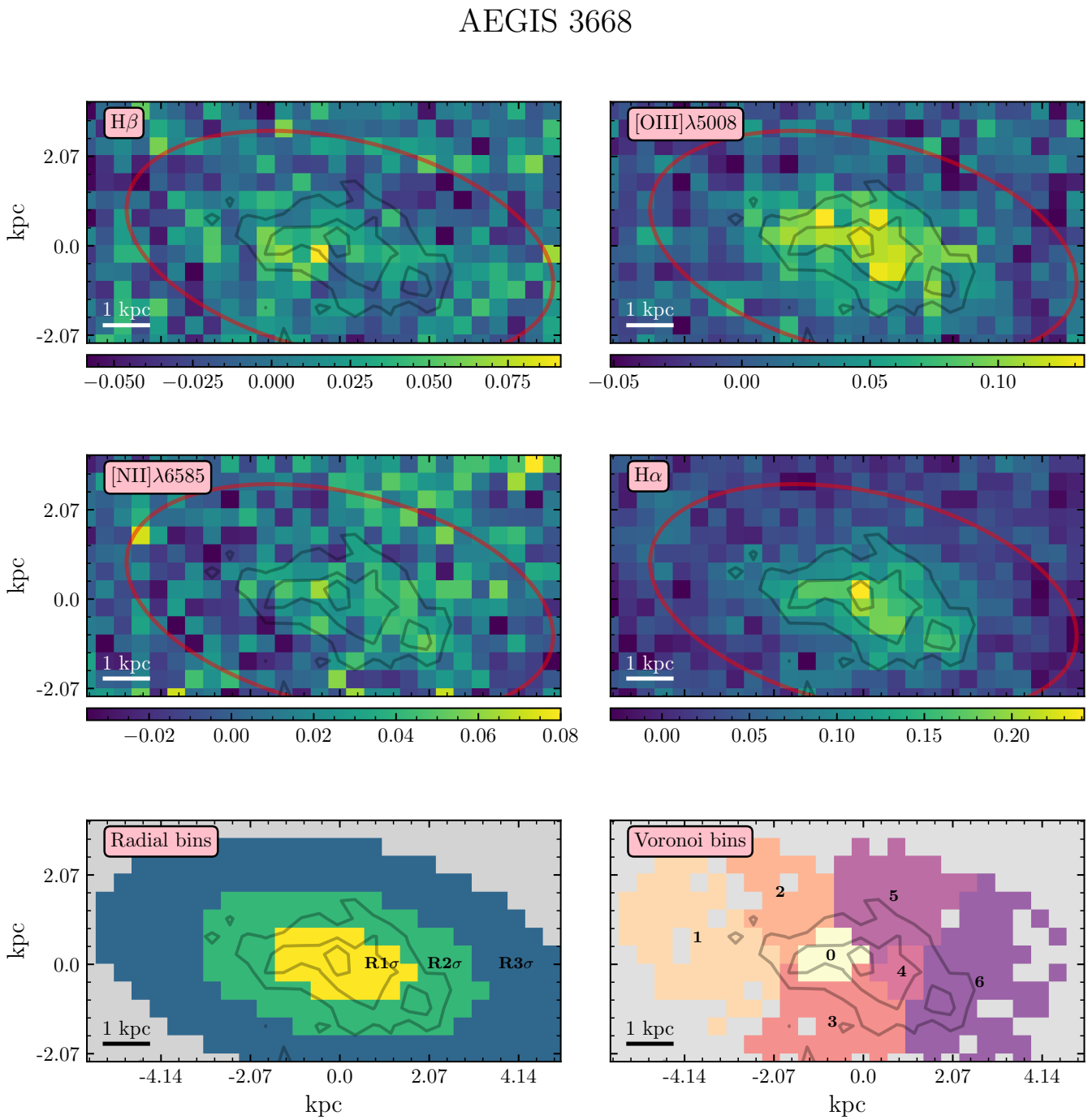

Figure 3. Emission line flux maps and spatial binning maps for AEGIS 3668, as in Fig. 1.

Since both groups of emission lines should trace roughly the same gas, we flagged fits where the velocity shift or broadening width in the lower S/N data (H band) differed from that in the higher S/N data (K band) by more than 1σ of the fit error to ensure consistency of the kinematics between the groups of emission lines. The lower S/N data was then refitted using the same kinematic-fixing procedure as above.

As a final quality check, we ensured that all fitted fluxes exceeded three times the fitting error (3σ). Spectra that did not meet this criterion were flagged and 3σ upper-limits were quoted in subsequent analysis.

For the integrated spectrum of all spaxels in some of the objects, the center of the narrow component did not match the systemic redshift determined from the spectra obtained from the MOSDEF survey. We performed

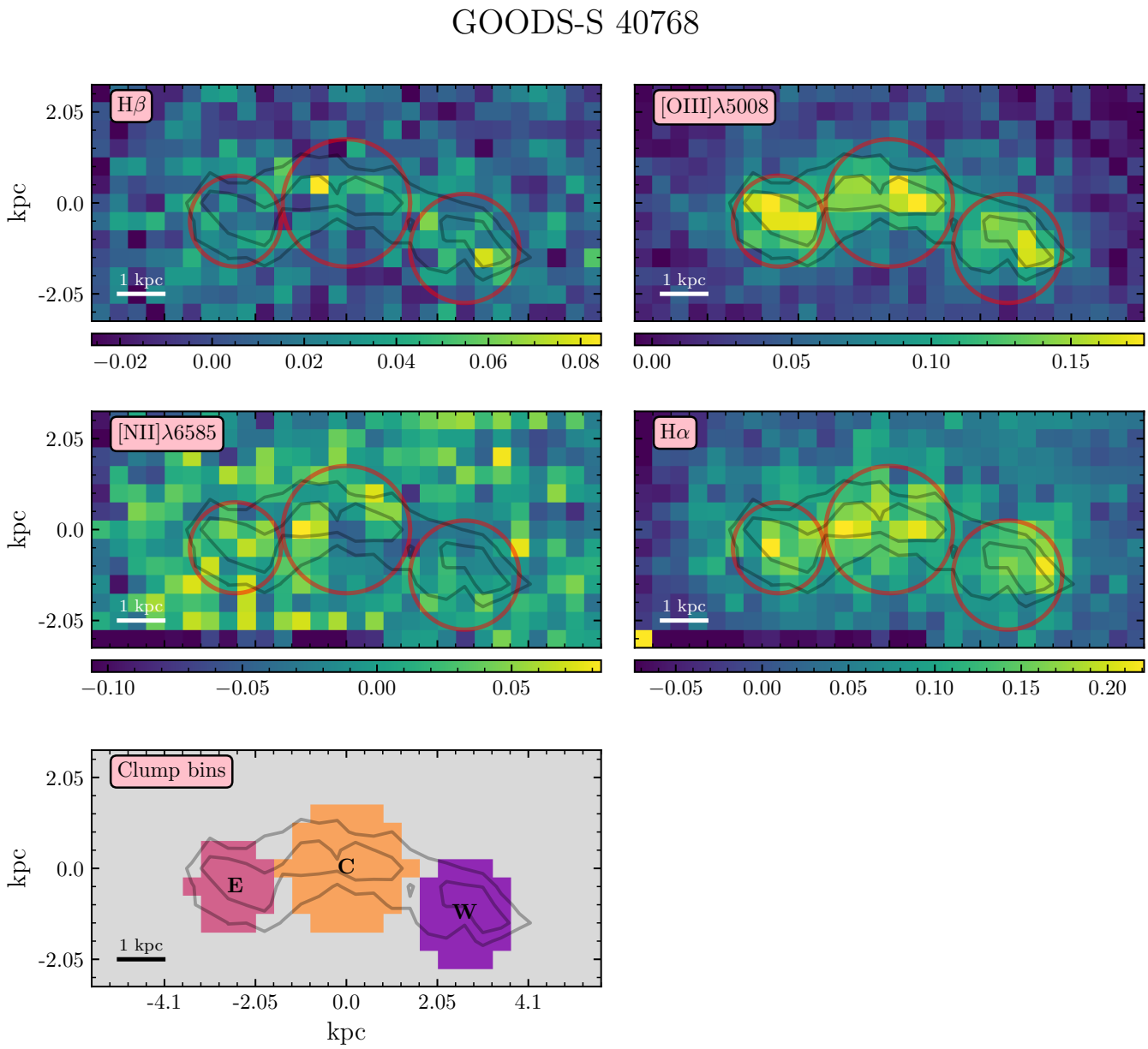

Figure 4. Emission line flux maps and spatial binning maps for GOODS-S 40768, as in Fig. 1. Here, the gray contours trace the higher S/N [O III]λ5008 flux map. Only three clump bins are defined for this galaxy due to its unusual morphology and lower S/N.

a two-component fit to the integrated spectra and redefined a systemic redshift based on the fitted center of the narrow component before performing fitting on the binned spectra. Furthermore, to ensure consistency in comparisons between the MOSFIRE and integrated OSIRIS spectra, we required that the MOSFIRE spectra adopt the preferred component fit of the corresponding integrated OSIRIS spectra.

Examples of all the above spectra and fitted profiles can be found in the Appendix.

3.2.2. *COSMOS 20062 clump*

From the fits for bins tracing the bright clump in COSMOS 20062 (Fig. 6), we find large systematic residuals, particularly in Voronoi Bin 7, which extends from the galaxy center to the clump to capture a larger spatial region. Although the two-component model appears to better encapsulate the [N II]$\lambda\lambda$6548, 6585+Hα profiles, the lower BIC values for the one-component model in both cases indicate that the simpler model is preferred. This preference is likely due to the lower S/N, which limits the addition of additional fitting parameters. While

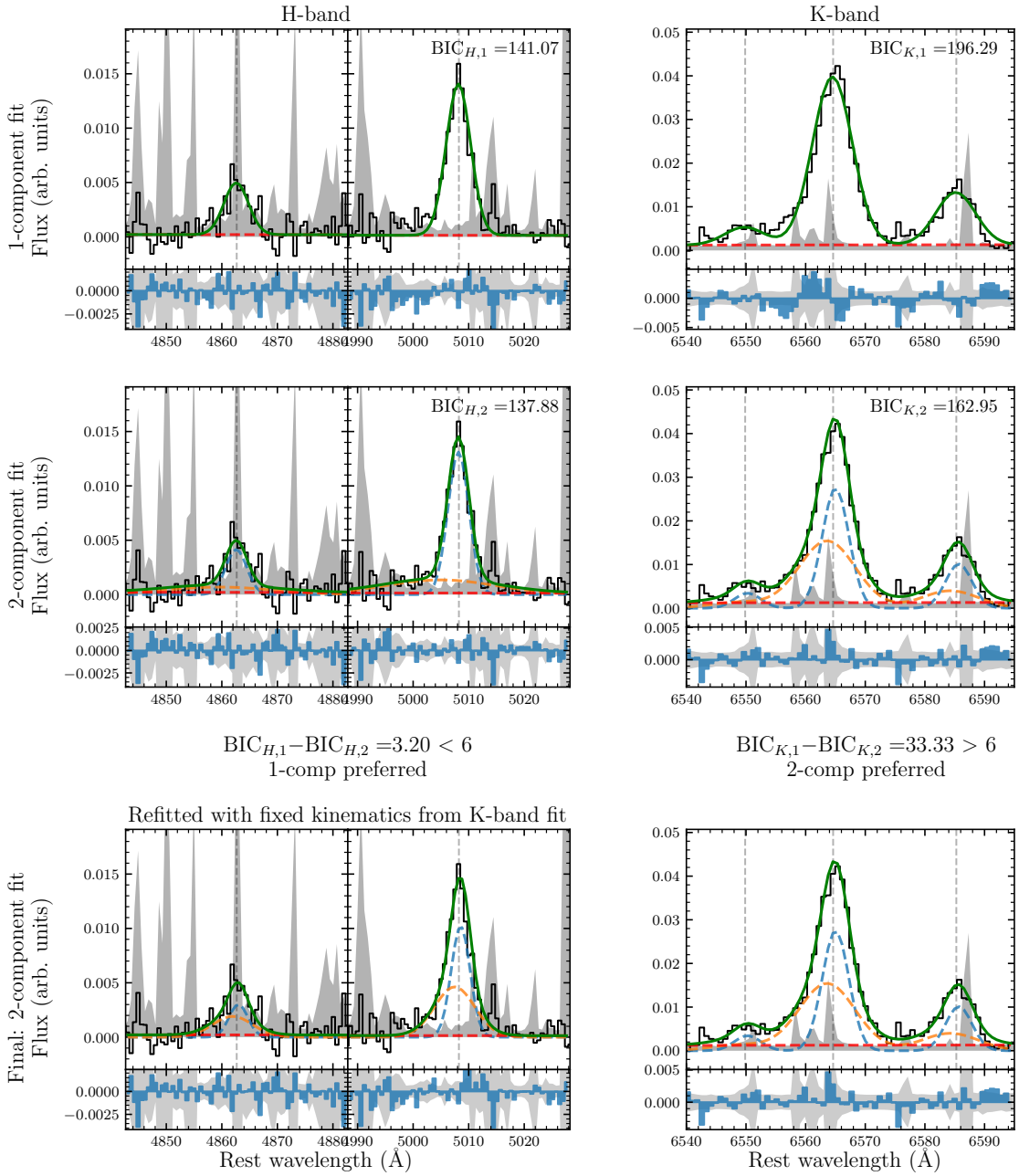

Figure 5. Example of emission line fitting routine for radial bin R1σ of COSMOS 20062. The left column shows the H band spectrum with emission lines Hβ and [O III]λ5008, while the right column shows the K band spectrum with the [N II]$\lambda\lambda$6548, 6585+Hα emission lines. The solid black curves represent the flux spectra and the gray shaded regions represent the error spectra. Each spectrum is fit with both a one-component (1-comp) and two-component (2-comp) model. For radial and clump bins, this fitting is performed for both H and K bands, while for Voronoi bins, it is applied only to the K band. The green solid curve represents the total fit, while the red dashed line shows the linear continuum fit around the emission lines. In the 2-comp model, the blue dashed line corresponds to the narrow component, and the orange line represents the broad component. The Bayesian Information Criterion (BIC) is used to assess model preference, with the more complex 2-comp model favored if its BIC value is at least 6 lower than that of the 1-comp model; otherwise, the 1-comp model is selected. For radial and clump bins, the preferred models are compared between the H and K bands. If the preference differs, the model from the band with the higher S/N is adopted. The spectrum in the lower S/N band is then refitted with its kinematics (Doppler shift and line broadening) fixed to the fitted values of the higher S/N band.

a more complex fit may be warranted by visual inspection, the available data do not provide strong statistical

justification for its adoption. Subsequent analysis will proceed using the one-component fits.

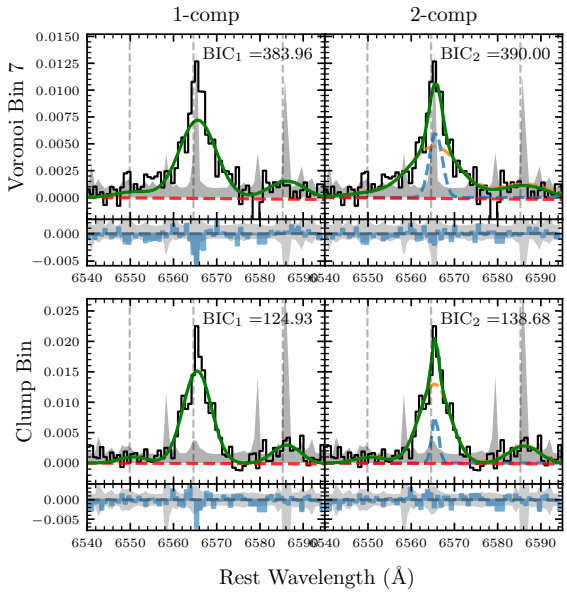

Figure 6. Spectral fits for bins tracing the bright clump in COSMOS 20062. The top row shows Voronoi Bin 7, which connects the galaxy center to the clump, while the bottom row shows a circular aperture with 0.1" radius centered on the clump. The left and right columns show the one- and two-component fits respectively. The color scheme follows that of Fig. 5. The BIC value for each fit is quoted at the upper-right corner of each panel. While the two-component model appears to fit better, the BIC analysis favors the one-component model, likely due to low S/N.

3.2.3. *COSMOS 19985 central spaxel*

From Fig. 7, it is evident that the best-fit one-component model determined by the fitting routine does not provide an adequate fit to the emission-line profiles. Thus, we introduced additional models, including a one-component fit with a broad Hα component, a two-component fit with a broad Hα component, and a three-component fit. The best-fit model was chosen to be the model with the lowest BIC value, with a minimum reduction of ΔBIC > 6 as compared to the original model to favor the new, more complex model. This analysis was conducted for all galaxies with Voronoi binning. Among them, only COSMOS 19985 exhibited spectra where one of these new models yielded the minimum BIC (see Fig. 23). Even in this case, the preference for a more complex model was limited to Voronoi Bin 0 (i.e. the central-most spaxel), where the two-component fit with a broad Hα component model was favored, as highlighted in Fig. 7. We quote measurements from the two-component plus broad Hα fit in subsequent analysis.

4. RESULTS

The integral field spectroscopic data obtained with OSIRIS provide crucial new insight into the spatial variations of galaxy properties. After fitting the emission-line profiles and applying two different binning methods, we can investigate how emission line flux ratios vary across different regions of each galaxy, allowing us to probe the nature of the ionization mechanisms shaping the ISM. In particular, we focus on the key emission lines [O III]λ5008, Hβ, [N II]λ6585, and Hα, examining how their flux is distributed between narrow and broad components and how these flux ratios change with radial distance. The following sections explore these spatial trends, leveraging emission-line diagnostics to gain insight into the ISM physical conditions within our galaxy sample.

4.1. *BPT diagrams*

One of the most widely used emission-line diagnostic tool for identifying the ionization mechanism of the ISM is the relationship between [O III]λ5008/Hβ and [N II]λ6585/Hα, introduced by Baldwin et al. (1981) (hereafter BPT). The placement of a galaxy on the BPT diagram helps determine whether its gas is photoionized by starlight, shocks, or an AGN.

First, we obtain the flux ratios [O III]λ5008/Hβ and [N II]λ6585/Hα from our fitted emission line profiles in the radial and clump bins that contain all four required emission lines. Since each ratio consists of emission lines within the same spectral region, we mitigate the need for flux calibration between bands or dust correction. Additionally, by separating the narrow and broad components, we can examine how emission is distributed between these components and assess radial variations in the narrow component, which primarily traces systemic gas and the ISM.

The BPT diagram in Fig. 8 display the [O III]λ5008/Hβ versus [N II]λ6585/Hα flux ratios for each galaxy, with solid points representing the narrow components of radial bins, and hollow points denoting the broad components if fitted. The color of each point (yellow, green, and blue) corresponds to the central bin and increasing radial annuli. Clump bins are also included for GOODS-S 40768 and COSMOS 20062. Star markers correspond to integrated galaxy spectra from different instruments: red for MOSFIRE and blue for OSIRIS. The narrow and broad components to the fit of COSMOS 19985 are shown, while the other galaxies were only fit with one component. To reveal the evolution of emission line ratios towards higher redshifts, we

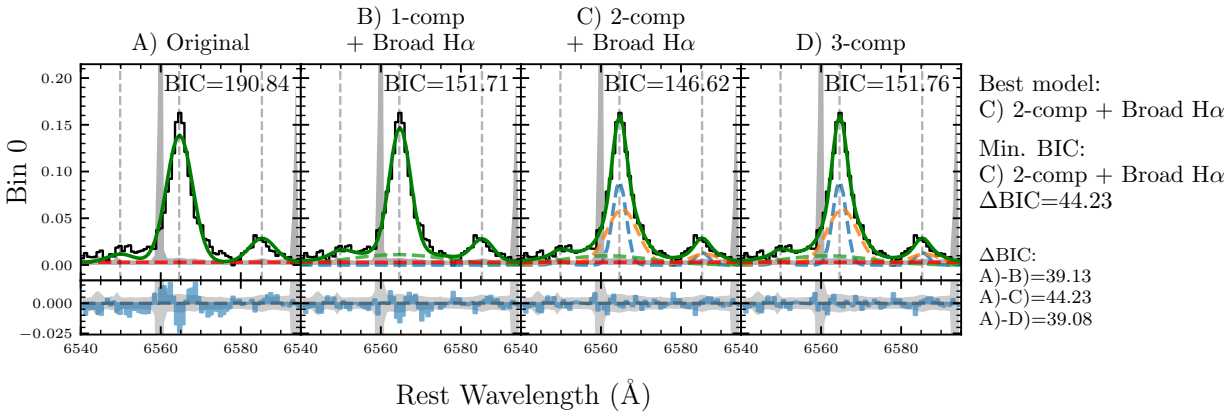

Figure 7. Spectral fits for Voronoi Bin 0 (i.e. center-most spaxel) in COSMOS 19985. The color scheme follows that of Fig. 5. The BIC value of each fit is quoted at the upper-right corner of each panel. Model A) is the one-component model preferred by the routine described in Section 3.2.1. Models B) and C) are one- and two-component profiles with an additional broad Hα Gaussian. Model D) is a three-component model. The best model, as determined by BIC analysis, is shown in the right column, along with the differences in BIC values between models.

include samples of $z \sim 0$ galaxies drawn from the Sloan Digital Sky Survey (SDSS) Data release 7 (Abazajian et al. 2009) and $z = 1.4 - 2.7$ galaxies from the AURORA survey (Shapley et al. 2025). These samples are plotted in the background of each BPT diagram as a grayscale histogram and as small red dots respectively.

For COSMOS 19985 in the top-left panel, we observe a ~ 0.3 dex decrease in log([O III]λ5008/Hβ) with increasing radius, while log([N II]λ6585/Hα) remains relatively constant. The MOSFIRE spectrum aligns well with the innermost radial bin, and the integrated OSIRIS point is similarly located near the central region. All the points lie above the $z \sim 0$ star-forming locus traced by the highest-density region of the grayscale histogram, but are roughly consistent with the $z = 1.4 - 2.7$ galaxies displayed as small red dots. Notably, the central R1σ bin lies on the Kewley et al. (2001) maximum starburst line, which could point towards additional ionizing mechanisms on top of pure star-formation ionization. However, given the known offset of high-redshift star-forming galaxies from the $z \sim 0$ locus (Steidel et al. 2014; Shapley et al. 2015), this elevated position does not provide compelling evidence for AGN activity.

For COSMOS 20062 in the top-right panel, the central bin R1σ required a two-component fit, which lowered the Hβ flux assigned to the narrow component, resulting in a non-detection in narrow Hβ flux and a 3σ lower limit for [O III]λ5008/Hβ. Regardless, we find no significant radial trend in [O III]λ5008/Hβ and a minor (< 0.2 dex) decrease in [N II]λ6585/Hα. Interestingly, the clump bin, which isolates the northwest region with high Hα surface brightness, exhibits lower [N II]λ6585/Hα but higher [O III]λ5008/Hβ. Since the clump bin falls mostly within the radial bin R3σ, its higher [O III]λ5008/Hβ ratio may increase the average value for [O III]λ5008/Hβ in bin R3σ and drive the overall small [O III]λ5008/Hβ variation. We also observe an offset between the MOSFIRE and integrated OSIRIS points, with the MOSFIRE point being closer to the clump and OSIRIS aligned with the other radial bins.

AEGIS 3668 (bottom-left panel) shows a similar trend to that of COSMOS 19985, with a ~ 0.3 dex decline in [O III]λ5008/Hβ and a minor decrease (< 0.2 dex) in [N II]λ6585/Hα with increasing radius. The MOSFIRE and integrated OSIRIS points are offset from the radial bins, but the [N II]λ6585/Hα upper limit suggests that the integrated OSIRIS spectrum may still lie within the range spanned by the binned points. Like the previous two COSMOS objects, all the radial bins follow the $z = 1.4 - 2.7$ galaxies and lie below the maximum starburst line.

In GOODS-S 40768 (bottom-right panel), the clumps span a wide range in [N II]λ6585/Hα, showing a distinct behavior from that of the radial bins of the other three galaxies. All the clump bins have relatively high [O III]λ5008/Hβ ratios of log([O III]λ5008/Hβ) ~ 0.7 as compared to what is observed in the other galaxies. Despite the higher [O III]λ5008/Hβ ratios, all points except for the center bin lie below the maximum starburst line. The MOSFIRE and integrated OSIRIS spectra agree well with the central, brightest clump, which is expected.

Fig. 9 shows a compilation of the radial and clump binned points from Fig. 8 on a summary BPT diagram. The radial bins for COSMOS 19985, COSMOS 20062, and AEGIS 3668 are connected by colored lines for clarity.

All four galaxies in our sample display the known BPT diagram offset towards higher [N II]λ6585/Hα and [O III]λ5008/Hβ for $z > 1$ galaxies. Moreover, among all our radially binned data points, only the center bins in COSMOS 19985 and GOODS-S 40768 lie slightly above the Kewley et al. (2001) maximum starburst threshold, suggesting that inclusion of an AGN is not required to explain the degree of ionization and excitation observed in these galaxies. Given that the properties of the central region in galaxies are most relevant in the search for AGNs, the fact that none of the central bins exceed the typical AGN identification threshold of [N II]λ6585/Hα = 0.5 (or log([N II]λ6585/Hα) = -0.3), as well as the lack of drastic differences in the line ratios of such central bins compared to bins at larger radii, suggest that there is no compelling evidence for AGN activity across the galaxies in any of the galaxies in our sample.

The central regions of galaxies are the most relevant for identifying AGNs. In our sample, none of the central bins exceed the typical AGN threshold of [N II]λ6585/Hα = 0.5 (or log([N II]λ6585/Hα) = -0.3). Additionally, the line ratios in these central bins are not significantly different from those at larger radii. Together, these findings suggest there is no compelling evidence for AGN activity in any of the galaxies we studied.

In general, we observe a decrease in [O III]$\lambda\lambda$4960, 5008/Hβ with increasing radius, while [N II]$\lambda\lambda$6548, 6585/Hα shows little to no significant variation, with at most a slight decrease. In particular, while the emission line ratios of each galaxy as a whole follow the general shape of the star-forming locus, the variation within individual galaxies appears nearly orthogonal to this trend, suggesting that a decrease in [N II]$\lambda\lambda$6548, 6585/Hα does not correspond to an increase in [O III]$\lambda\lambda$4960, 5008/Hβ within a galaxy.

4.2. *Radial variations in [N II]λ6585/Hα ratios*

From the Voronoi-binned K-band data, we obtained the [N II]λ6585/Hα flux ratios for the fitted line profiles in COSMOS 19985, COSMOS 20062, and AEGIS 3668. GOODS-S 40768 was omitted from this analysis due to its unusual morphology and low S/N. As mentioned in Section 3.1.2, the Voronoi-binning strategy recovers more spatial information than the radial bins used in the BPT diagram analysis, enabling us to more robustly examine spatial variations of emission line ratios.

Fig. 10 presents the [N II]λ6585/Hα ratios in each bin as a function of the distance from the luminosity-weighted center of each of the Voronoi bins to the center of the galaxy ellipse fit. To facilitate interpretation, we also show the conversion of [N II]λ6585/Hα to gas-phase metallicity for high-redshift galaxies, using the relation

$$12 + \log(\mathrm{O/H}) = 8.82 + 0.49 \times \log([\mathrm{NII}]\lambda6585/\mathrm{H}\alpha) \quad (1)$$

from Bian et al. (2018). Though this relation is calibrated for galaxies with metallicities spanning $7.8 < 12 + \log(\mathrm{O/H}) < 8.4$ and our analysis requires extrapolation up to $12 + \log(\mathrm{O/H}) \sim 8.6$, the uncertainties from extending the relation slightly above the metallicity range should be small in comparison to those resulting from $z \sim 0$ calibrations. Furthermore, as the analysis mainly focuses on metallicity gradients, the absolute value calculated from the relation matters less than the relative differences between data points. The small solid points represent the narrow component, while hollow points correspond to the broad component, and arrows indicate 3σ upper limits. Points from radial bins are also shown with larger markers. The yellow, green, and blue markers represent the R1σ, R2σ, and R3σ bins, following the marker shapes and color schemes in Fig. 8.

We performed a linear fit using the Bayesian regression method implemented in `linmix` (Kelly 2007), which accounts for non-detections through an MCMC-based approach. The plotted lines in the panels in Fig. 10 show the median fit to the narrow component points, with the bottom-right panel displaying the fits along with the corresponding 16th-84th percentile error regions. Broad component points are included for reference but were not fitted. The median slope m and intercept b of the fit samples for the narrow components, along with their standard deviations, are reported at the bottom of the panels. In AEGIS 3668, due to a high number of non-detections, we simply connected the two detected points with a dotted line and fit errors are not included, thus any interpretation should be made with caution.

In COSMOS 19985 (top-left panel), the narrow component [N II]λ6585/Hα ratios exhibit a slight positive radial gradient of $0.03^{+0.06}_{-0.06}$ dex kpc^{-1}, but, given the large uncertainty, there is no statistically significant preference for a positive or negative trend. The mean [N II]λ6585/Hα value across detected narrow component bins is log([N II]λ6585/Hα) = -0.66 ± 0.08, corresponding to a metallicity of 8.49 ± 0.04. Broad components are detected in 5 bins, spanning a smaller ~ 1 kpc radial range. In general, the [N II]λ6585/Hα values of these broad components are lower than those measured in the narrow component, with a median of log([N II]λ6585/Hα) = -0.71 ± 0.23. However, given the small number of data points and the large span of ~ 0.4 dex, we did not attempt to fit a linear trend to the broad component.

In COSMOS 20062 (top-right panel), the narrow component ratios suggest a negative gradient of

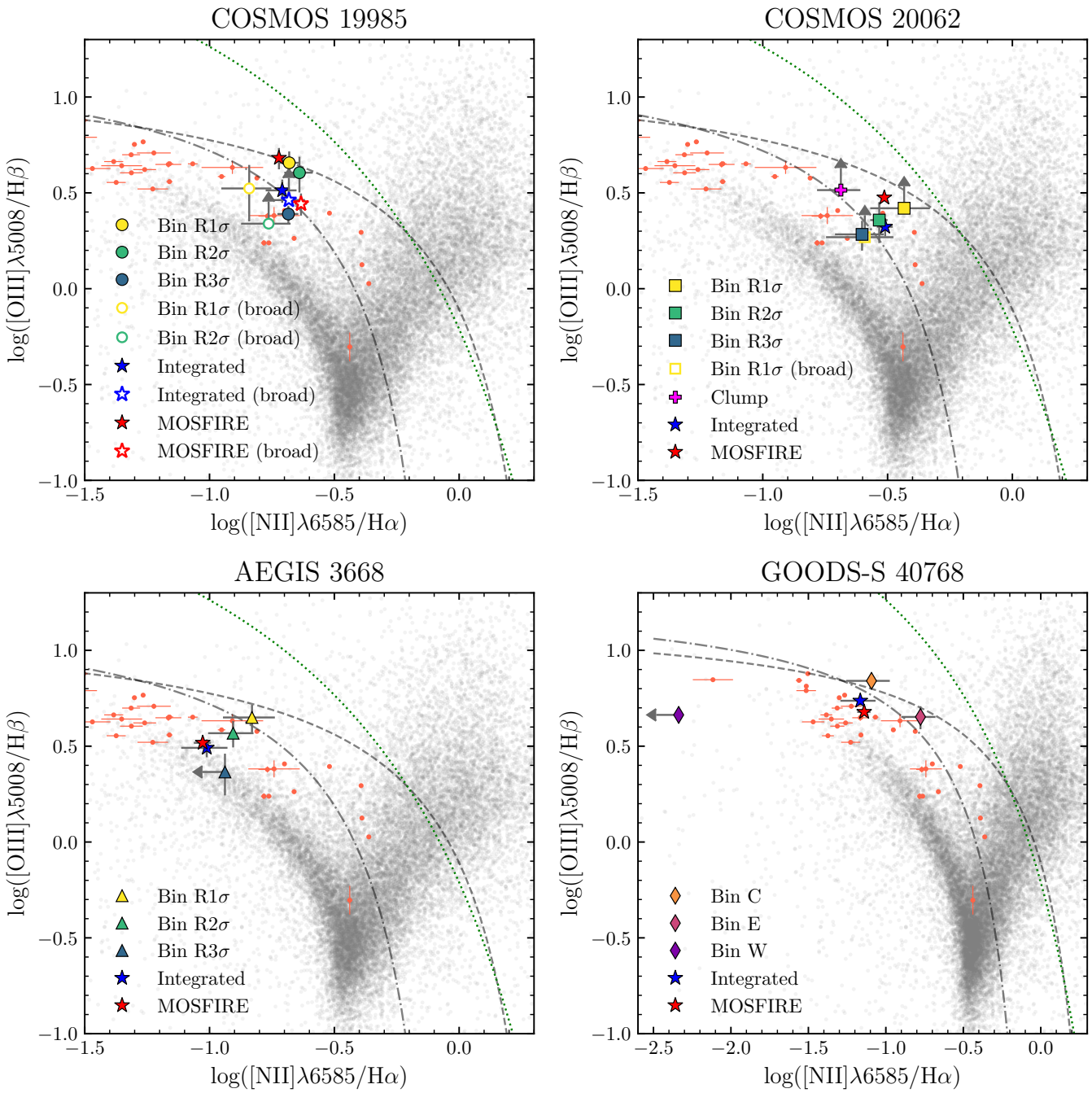

Figure 8. BPT emission-line diagnostic diagrams for each galaxy: COSMOS 19985 (top left), COSMOS 20062 (top right), AEGIS 3668 (bottom left), and GOODS-S 40768 (bottom right). In each panel, the background grayscale histogram shows the distribution of local SDSS galaxies and the small red dots are $z = 1.4-2.7$ galaxies from Shapley et al. (2025). The dashed curve is the "maximum starburst" line from Kewley et al. (2001), while the dot-dashed curve is the empirical AGN/star-formation threshold at $z \sim 0$ from Kauffmann et al. (2003) and the green dotted curve is the threshold for high-redshift galaxies from Scholtz et al. (2023). Solid points indicate the narrow component fit in radial bins, with yellow, green, and blue corresponding to the central bin and increasing radial annuli. For bins that include a broad component, the points are displayed with hollow markers, with the same marker shapes and color scheme. Clump bins are also included for GOODS-S 40768 and COSMOS 20062. Star markers correspond to integrated galaxy spectra from different instruments: red for MOSFIRE and blue for OSIRIS. The narrow and broad components to the fit of COSMOS 19985 are shown, while the other galaxies were only fit with one component. Arrows indicate 3σ upper or lower limits.

$-0.13^{+0.09}_{-0.17}$ dex kpc^{-1}, but the large uncertainty once again renders the slope insignificant. This apparent

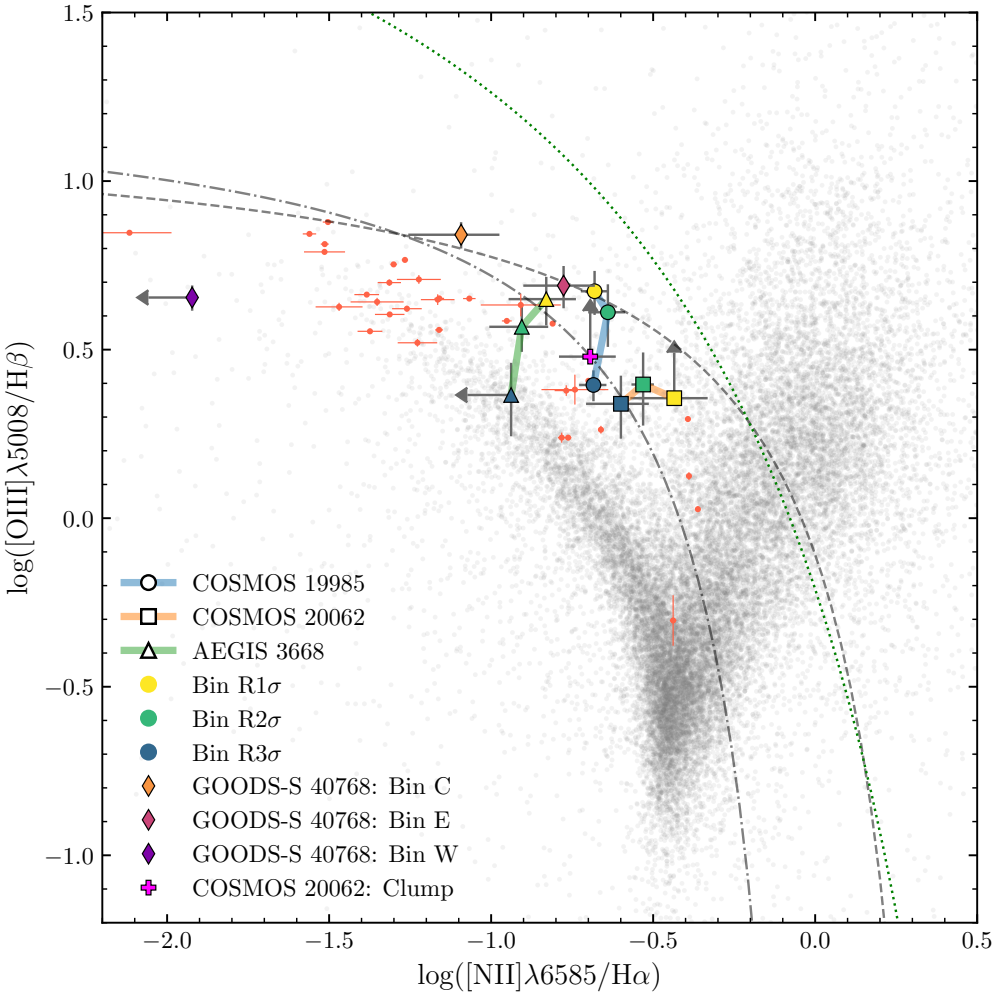

Figure 9. Summary of BPT emission-line diagnostic diagrams for all galaxies in this study. This figure includes all radial and clump bins from Fig. 8, following the same marker shapes and color scheme. Radial bins for each galaxy are connected by colored lines for clarity. The background grayscale histogram represents the distribution of local SDSS galaxies, small red dots are $z = 1.4 - 2.7$ galaxies from Shapley et al. (2025), and the dotted and dot-dashed curves are from Kewley et al. (2001) and Kauffmann et al. (2003) respectively. Arrows indicate 3σ upper or lower limits.

trend is likely skewed by the low point at ~ 2.8 kpc, corresponding to Voronoi bin 4 (see Fig. 20), where the [N II]λ6585 line flux is particularly weak. The non-detection at the largest radius corresponds to the bin containing the clump described in Section 3.1.1, where the large fitting uncertainties drive down the S/N. The mean [N II]λ6585/Hα ratio for the narrow component is $\log([\mathrm{N\,II}]\lambda6585/\mathrm{H}\alpha) = -0.55 \pm 0.12$, corresponding to a metallicity of 8.55 ± 0.06.

All the bins in AEGIS 3668 (bottom-left panel) were fitted by a one-component model. However, due to the low S/N of the spectra, 5 out of the 7 [N II]λ6585/Hα ratios were non-detections. Despite the high fraction of non-detections, the two detected points differ by less than 0.05 dex over a radial distance of nearly 2 kpc, suggesting that there is no significant metallicity gradient. Additionally, the non-detections are randomly distributed around the detected points, further supporting the lack of a strong radial trend. The mean of the detections is $\log([\mathrm{N\,II}]\lambda6585/\mathrm{H}\alpha) = -0.85 \pm 0.02$, corresponding to a metallicity of 8.40 ± 0.01, lower than that of COSMOS 19985 and COSMOS 20062.

The [N II]λ6585/Hα flux ratios measured from the radially-binned spectra also follow those from the Voronoi-binned spectra very closely. Particularly, for COSMOS 20062, points from the radial bins trace the main sequence of Voronoi-binned points, showing that the low point at ~ 2.8 kpc is an outlier as compared to the general metallicity trend of the rest of the galaxy. The metallicity gradient measured for COSMOS 20062 is thus driven more negative by the low [N II]λ6585/Hα flux ratio of Voronoi bin 4.

All in all, the [N II]λ6585/Hα ratios do not show clear radial trends across the galaxies in our sample, consistent with the lack of strong radial variation seen in the BPT diagrams in Section 4.1. Across all three galaxies, the [N II]λ6585/Hα ratios at the center-most regions remain below log([N II]λ6585/Hα) ~ -0.3 (or [N II]λ6585/Hα $\sim$ 0.5), a commonly used threshold for distinguishing AGN ionization from star formation (e.g., Shapley et al. 2015). The absence of higher [N II]λ6585/Hα ratios at small radii indicates that the central regions are not strongly influenced by AGN ionization, and are, instead, more consistent with excitation by star formation.

4.3. *Radial variations in ([O III]λ5008/Hβ)/([N II]λ6585/Hα) ratios*

Similar to the analysis in Section 4.2, the ([O III]λ5008/Hβ)/([N II]λ6585/Hα) (O3N2) ratio serves as a metallicity indicator. From the radially-binned H- and K-band data, we obtained O3N2 ratios for the fitted line profiles in COSMOS 19985, COSMOS 20062, and AEGIS 3668 for metallicity gradient analysis.

Fig. 11 shows the O3N2 ratios in the radial bins as a function of the distance from the bins to the center of the galaxy ellipse fit. The distance is defined as the center of the galaxy ellipse fit for R1σ, and 1.5 and 2.5 times the semi-major axis of the ellipse fit for R2σ and R3σ. The conversion of O3N2 to gas-phase metallicity for high-redshift galaxies, using the relation

$$12 + \log(\mathrm{O/H}) = 8.97 - 0.39 \times \log(\mathrm{O3N2}) \qquad (2)$$

from Bian et al. (2018). Again, we note that the highest metallicity in our sample exceeds the upper limit of 12 + log(O/H) = 8.4 of this calibration by 0.2 dex. Though extrapolation is needed, we determine that analysis performed based on this relation is still more robust than that based on $z \sim 0$ calibrations. The data points follow the marker shapes and color schemes in Fig. 8, where solid points denote the narrow component and hollow points show the broad component if fitted. Arrows indicate 3σ upper limits. The O3N2 axes are inverted to reflect the inverse relationship between O3N2 and metallicity.

For COSMOS 19985, we fit the narrow component trend with a linear model using a least-squares approach. Given that only two radial bins in each of COSMOS 20062 and AEGIS 3668 have detections in O3N2, we simply connected the two detections with a straight line. These linear fits are overplotted as dotted lines in each panel. Due to the small number of bins and detections, the fitted slope m and intercept b values shown in each panel should be interpreted with caution.

In COSMOS 19985 (top-left panel), the narrow component O3N2 ratios show a negative trend of $\sim -0.10 \pm 0.02$ dex kpc^{-1}, which gives a slightly positive metalicity gradient of $\sim 0.040 \pm 0.008$ dex kpc^{-1}, similar to that derived from the [N II]λ6585/Hα ratio in Section 4.2. The mean O3N2 value across detected narrow component points is log(O3N2) = 1.22 ± 0.11, which corresponds to a metallicity of 8.49 ± 0.04 and is in agreement with [N II]λ6585/Hα-derived values.

The narrow component O3N2 ratios in COSMOS 20062 show a flat gradient between the two detections in R2σ and R3σ. The inferred flat metallicity gradient is consistent with the trend found in the [N II]λ6585/Hα analysis for radial bins and the majority of Voronoi bins. The mean O3N2 ratio among the two detected points is log(O3N2) $\sim$ 0.89, corresponding to a metallicity of $\sim$ 8.62. The mean O3N2-based metallicity is $\sim$ 0.1 dex higher than the [N II]λ6585/Hα-derived value.

For AEGIS 3668, the O3N2 gradient and metallicity gradient from the two detections in R1σ and R2σ are flat, similar to that measured from the [N II]λ6585/Hα ratio. The mean O3N2 ratio among the two detected points is log(O3N2) $\sim$ 1.48, corresponding to a metallicity of $\sim$ 8.39 which is consistent with the metallicity calculated with the [N II]λ6585/Hα diagnostic.

All in all, the O3N2-based gas-phase metallicities and metallicity gradients corroborate those derived using the [N II]λ6585/Hα calibrations.

5. DISCUSSION

5.1. *AGN diagnostics*

We present spatially resolved IFU data on four galaxies at $z \sim 2$, previously observed with integrated spectroscopy as part of the MOSDEF survey. The classification of these galaxies as star-forming or AGN based on emission line ratios is complicated by the known offset of the high-redshift star-forming locus on the BPT diagram, which shifts towards higher [O III]λ5008/Hβ and [N II]λ6585/Hα values relative to the sequence defined by local star-forming galaxies (e.g., Steidel et al. 2014; Shapley et al. 2015). As discussed previously, among many possible explanations, it appears that this BPT offset is driven by a harder ionizing spectrum at fixed nebular metallicity for chemically-young, high-redshift galaxies (e.g., Steidel et al. 2016; Cullen et al. 2021; Shapley et al. 2025).

The offset of the $z \sim 2$ star-forming locus causes many high-redshift star-forming galaxies to occupy the "composite" region of the BPT diagram based on calibrations at $z \sim 0$. In this region, AGN and star-formation contributions are difficult to disentangle. This ambiguity

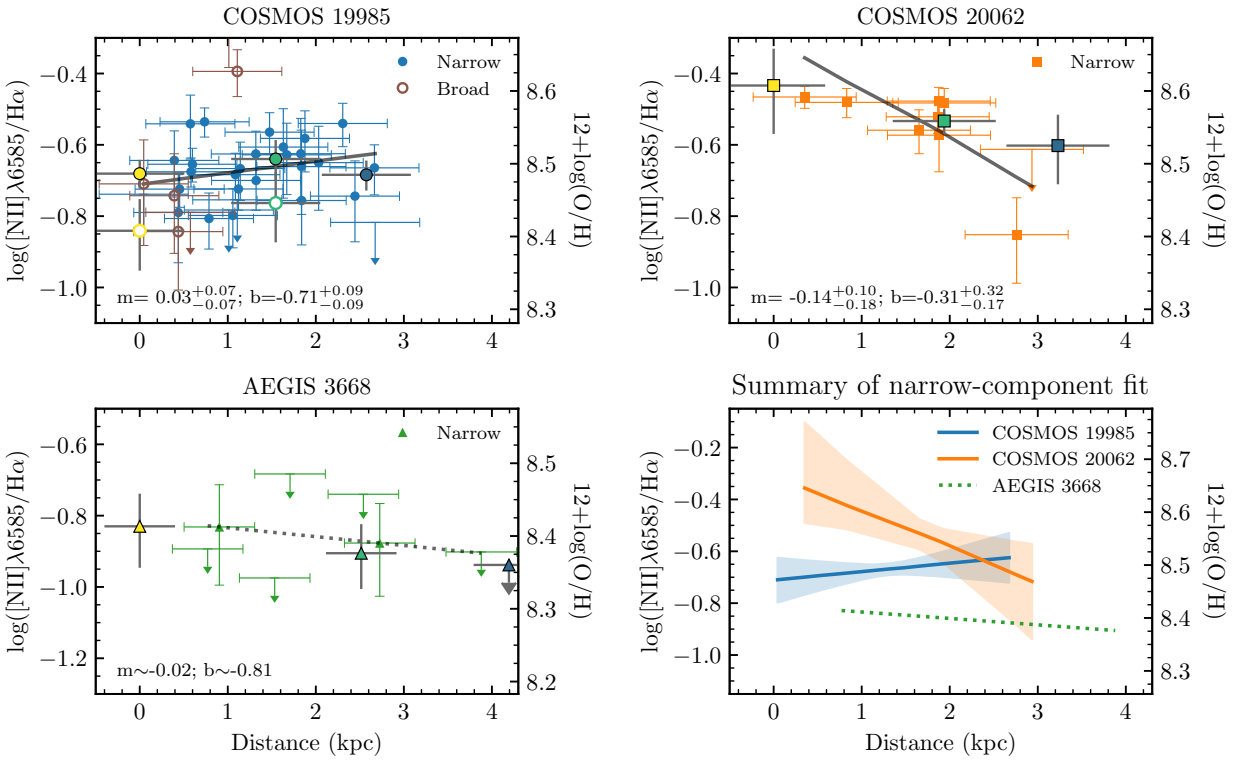

Figure 10. [N II]λ6585/Hα flux ratio vs. distance for Voronoi-binned fits of COSMOS 19985 (top-left), COSMOS 20062 (top-right), and AEGIS 3668 (bottom-left). The bin distances are from the luminosity-weighted center of each bin to the center of the galaxy ellipse fit. Small solid points represent the narrow component, hollow points are the broad component, and arrows indicate 3σ upper limits. Points from radial bins are also shown, following the marker shapes and color schemes in Fig. 8. The solid lines show the median linear fits to the narrow component, with the bottom-right panel overlaying all the fitted lines and their 16th–84th percentile error regions. Median slopes and intercepts, along with errors, are reported at the bottom of the COSMOS 19985 and COSMOS 20062 panels. The values quoted for AEGIS 3668 parametrize the dotted line connecting the two detected points, and thus should be interpreted with caution.

can be seen in our sample, with COSMOS 19985 and COSMOS 20062 being classified as star-forming or as hosting AGN based on their integrated spectra in different studies (Sanders et al. 2023; Leung et al. 2017). To make matters even more complicated, emission line ratios obtained from integrated galaxy spectra can differ from those measured from smaller apertures focused on central regions in galaxies that host a weak AGN. Wright et al. (2010) demonstrated this effect for distant-galaxy spectra, measuring a ~ 0.3 dex increase in both log([O III]λ5008/Hβ) and log([N II]λ6585/Hα) for a $z = 1.6$ galaxy's "concentrated" spectrum relative the integrated measurements. These discrepancies and uncertainties highlight the need for high-redshift calibrations of emission line diagnostics, as well as spatially-resolved observations to better isolate the ionization mechanisms in the central regions of galaxies where AGN activity is expected to have the strongest influence on line ratios.

Therefore, in Section 4.1, we primarily used two demarcations lines to interpret the nature of the galaxies in our sample: the maximum starburst line from Kewley et al. (2001) that sets a theoretical threshold for ionization from pure star formation, and the empirical AGN threshold based on observations of $z < 5$ galaxies from Scholtz et al. (2023). In Scholtz et al. (2023), high-redshift Type 2 AGN are seen to occupy similar spaces as star-forming galaxies, so the latter boundary serves as a conservative limit above which no star-forming galaxies are found. We find that all but two of our data points fall below the maximum starburst line and that all points lie well below the Scholtz et al. (2023) limit.

We observe an increase in [O III]λ5008/Hβ ratio in the center-most bin R1σ in COSMOS 19985 as compared to the value obtained from the integrated OSIRIS spectrum. Similarly, we see an increase in both [O III]λ5008/Hβ and [N II]λ6585/Hα for AEGIS 3668. This trend reflects the effect of aperture size discussed

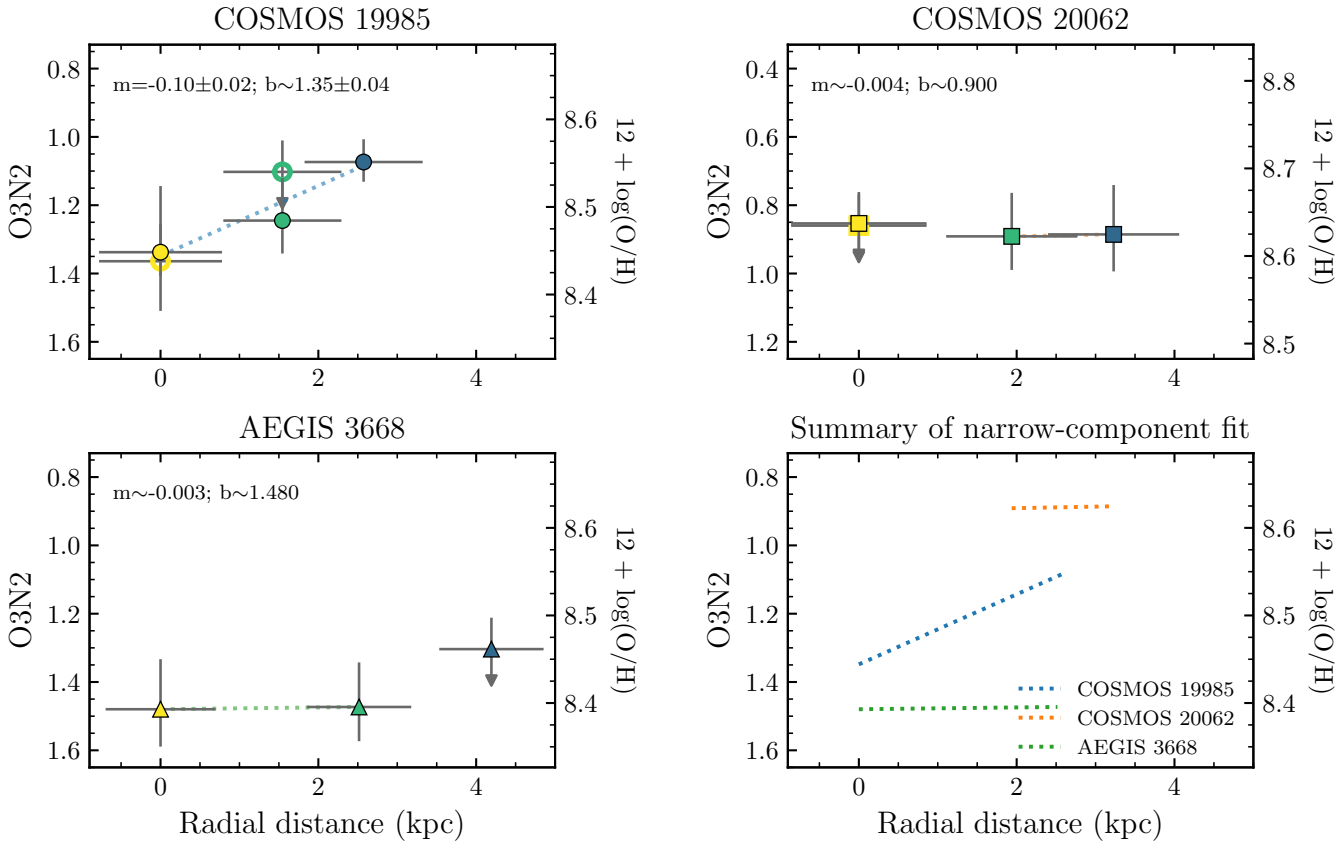

Figure 11. ([O III]λ5008/Hβ)/([N II]λ6585/Hα) O3N2 ratios vs. distance for radially-binned fits of COSMOS 19985 (top-left), COSMOS 20062 (top-right), and AEGIS 3668 (bottom-left). The bin distances are from the mid-point of each radial annuli to the center of the galaxy ellipse fit. Solid points represent the narrow component, hollow points are the broad component, and arrows indicate 3σ upper limits. The marker shapes and color schemes follow those in Fig. 8. The dotted lines show the linear fits to the narrow component, with the bottom-right panel overlaying all the fitted lines. Given the small number of bins and detections, the fitted slope and intercept values shown in each panel should be interpreted with caution.

above and in Wright et al. (2010), where the contributions of an embedded weak AGN could be drowned out by the light of a predominantly star-forming galaxy in an integrated spectrum of the galaxy. While smaller apertures focused on the central regions of a galaxy, or bin R1σ in our analysis, can help isolate the contribution of an AGN if present, our data show that none of the central bins exhibit line ratios elevated beyond the maximum starburst line. Combined with the fact that our data points scatter around those from $z = 1.4 - 2.7$ galaxies from Shapley et al. (2025) and that the centermost, finer Voronoi bins have [N II]λ6585/Hα < 0.5, there is no compelling evidence for AGN activity in our sample, and the AGN scenario is disfavored.

5.2. *Notable deviations and unusual trends in the BPT diagram*

As mentioned in Section 4.1, the center radial or clump bins of COSMOS 19985 and GOODS-S 40768 lie on or slightly above the maximum starburst threshold. In COSMOS 19985, the central spaxel within radial bin R1σ as probed by Voronoi bin 0 required a broad Hα component with FWHM velocity ~ 1200 km s^{-1} to fit the emission line profile (see Section 3.2.3). However, the broad Hα flux is barely detected, with S/N just above 3, making it unlikely that we would detect a corresponding broad [N II]λ6585 component even if present. Additionally, the high star formation rate (SFR) surface density of 18.5±0.7 M$_\odot$ yr^{-1} kpc^{-2} measured by Sanders et al. (2023) significantly exceeds the 0.1 M$_\odot$yr^{-1} kpc^{-2} requirement for star formation-driven outflows. Combined with the observed [N II]λ6585/Hα $\ll 0.5$ in the central spaxel, these observations point towards complex outflow kinematics rather than AGN activity in COSMOS 19985.

GOODS-S 40768 also exhibits an anomalous feature, with the center clump bin showing the most significant offset above the maximum starburst line among our sample (see Fig. 9). Though strong central AGN activity is unlikely, further observations of additional emission

lines (e.g. [O I], [Si II], [Ne III], [O II]) are needed to better characterize the ionization conditions in each of the clumps and determine whether the deviation in the center clump is due to unusual ISM conditions, a hidden AGN contribution, shocks from accreting gas, or other mechanisms.

Beyond individual points above the maximum starburst line, we also observe a notable internal trend in our galaxies with radial binning where higher [O III]λ5008/Hβ ratios do not correspond to lower [N II]λ6585/Hα. This pattern diverges from typical expectations for star-forming galaxies and suggests the presence of additional physical processes influencing the observed line ratios. However, further data are needed to confirm and interpret this trend.

5.3. *Radial metallicity gradients*

In Sections 4.2 and 4.3, we investigated radial trends in [N II]λ6585/Hα and O3N2 ratios measured from Voronoi-binned and radially-binned spectra to infer the gas-phase metallicity gradients for our galaxies. The mean [N II]λ6585/Hα ratios measured for COSMOS 19985 and COSMOS 20062 are consistent with those reported in Sanders et al. (2023), though our inferred metallicity for COSMOS 19985 is 0.5 dex higher than the direct metallicity obtained in their work. While the absolute metallicity scaling inferred from [N II]λ6585/Hα may be subject to systematic offsets at high redshifts, our analysis focuses on the relative gradient rather than the absolute values.

Among the three galaxies on which we performed Voronoi binning, we find our targets exhibit mostly flat radial gradients in gas-phase metallicity, with COSMOS 19985 and AEGIS 3668 showing gradients within 0.02 dex kpc^{-1} positive and negative from flat respectively. The steepest gradient of -0.13 dex kpc^{-1} observed in COSMOS 20062 has a large uncertainty that can shift the slope to be consistent with zero slope. The metallicity gradients calculated from the O3N2 diagnostic with the fewer, but higher S/N radially-binned data, also corroborate the flat trends revealed by the [N II]λ6585/Hα ratio analysis.

Flat gas-phase metallicity gradients have been widely reported for star-forming galaxies at $z \sim 2$ and are commonly described by efficient radial mixing driven by supernova feedback and galactic outflows (e.g., Gibson et al. 2013; Ma et al. 2017; Curti et al. 2020; Förster Schreiber et al. 2018). A similar prevalence of flat gradients has been observed in slitless HST grism spectroscopy, where 54 out of 76 galaxies at $z \sim 2$ show metallicity gradients consistent with flat within 2σ uncertainties (Wang et al. 2020). However, there is a significant diversity of gradients in the literature, with values ranging from -0.2 to $+0.2$ dex kpc^{-1} (Wang et al. 2020). Some studies have found steep negative gradients in lensed galaxies at $z \sim 2$, suggesting inside-out growth (Jones et al. 2010, 2013). Others report a high fraction of positive (or inverted) gradients in overdense regions as compared to the fractions found in blank fields at $z \sim 2$, possibly driven by "cold-mode" accretion of metal-poor gas into central regions of galaxies (Wang et al. 2019; Li et al. 2022). The large scatter in observed metallicity gradients at $z \sim 2$ may reflect the diversity of physical mechanisms shaping metallicity distributions at this epoch.

Cosmological simulations have similarly found a wide range of metallicity gradients at high redshift, depending on the strength of stellar feedback and the timescales of metal redistribution. High-resolution simulations with strong stellar feedback tend to predict flatter gradients at high-redshift, as outflows efficiently mix metals throughout the ISM (e.g., Ma et al. 2017; Tissera et al. 2019). In contrast, lower-resolution simulations with weaker subgrid feedback prescriptions tend to produce more negative gradients, as metals remain more centrally concentrated (e.g., Gibson et al. 2013; Hemler et al. 2021). Additionally, Ma et al. (2017) demonstrated that, at high redshift, short-timescale variations in metallicity gradients can occur due to episodic starburst activity. During a starburst phase, infalling metal-poor gas can temporarily steepen a negative gradient, while subsequent outflows redistribute metals, flattening the gradient. Over time, metal recycling via galactic fountains can re-establish a negative gradient. This effect is particularly pronounced in low-mass, high-SFR galaxies where stellar feedback is most efficient. Given the high SFR of our galaxies and relatively flat metallicity gradients, our observations are consistent with a scenario with significant radial mixing and redistribution of metals by star formation-driven outflows.

Furthermore, correlations between metallicity gradients and global galaxy properties also vary across studies. In overdense environments, such as galaxy clusters or protoclusters, metallicity gradients tend to be flat or inverted, with evidence of anticorrelation between metallicity gradients and global metallicities (Li et al. 2022). Curti et al. (2020) also found that in galaxies with significantly inverted (positive) metallicity gradients, regions with higher SFR surface density tend to have weaker (less positive) metallicity gradients, while regions with lower SFR surface density tend to have stronger (more positive) metallicity gradients. This indicates an anticorrelation between metallicity gradients and SFR surface density on local scales, sug-

gesting episodes of pristine gas accretion or strong radial flows. On the other hand, field galaxies tend to have flat or slightly negative gradients, with no significant correlation between metallicity gradients and global galaxy properties, kinematics, or AGN activity (Förster Schreiber et al. 2018). Since our targets are field galaxies, their flat gradients may reflect the lower environmental influence expected in field regions. Along with the detection of gas flow components in COSMOS 19985 and COSMOS 20062, our results potentially highlight the role of internal processes such as outflows and radial mixing over global environmental effects in the flattening of gas-phase metallicity gradients.

Another factor that impacts measured metallicity gradients is insufficient spatial sampling. Low spatial resolution can artificially flatten metallicity gradients (e.g., Yuan et al. 2013; Acharyya et al. 2020). While some of our inner Voronoi bins cover sub-kpc regions, most outer bins span areas larger than 1 kpc^2, which can contribute to the flattening of radial trends. This effect is most pronounced in COSMOS 20062 and AEGIS 3668, where coarse Voronoi binning was necessary to achieve sufficient S/N. However, nearly all Voronoi bins in COSMOS 19985 have sub-kpc spatial resolution, ensuring that any intrinsic metallicity gradient would be clearly detected. The fact that COSMOS 19985 still exhibits a flat metallicity gradient strongly indicates that this result is not an artifact of limited spatial resolution, but rather a true feature of the galaxy.

6. CONCLUSION

High-redshift galaxies have different ISM physical conditions from those found in the local universe. While these differences limit the reliability of locally calibrated emission line ratio diagnostics, by studying the variations, we can gain insight into the mechanisms that drive galaxy evolution and shape the ISM during this epoch of peak star formation.

In this work, we conducted a spatially resolved analysis of four galaxies at $z \sim 2$ selected from the MOSDEF survey for their potentially composite nature from BPT diagnostics and possible evidence of strong gas flow. Our analysis of IFU data revealed that the [N II]λ6585/Hα and [O III]λ5008/Hβ ratios in the central $\sim$ 1 kpc region of our galaxies are not high enough to provide compelling evidence for AGN activity, and instead supports the interpretation that these galaxies are undergoing intense star formation, capable of driving strong outflows. Furthermore, the gas-phase metallicity gradients, as probed by [N II]λ6585/Hα ratios, appear to be flat. This result aligns with previous findings at similar redshifts and suggests that efficient radial mixing shapes the distribution of metals within the ISM during cosmic noon.

Beyond these global trends, we identified intriguing features within individual galaxies, including radial BPT variations that deviate from the expected star-forming sequence and localized regions that lie slightly above the maximum starburst line. In order to fully disentangle the ionizing mechanisms and physical processes responsible for the deviations above the theoretical maximum of ionization from pure star-formation, we require data on additional emission lines such as [O I], [Si II], [Ne III], and [O II]. Flux ratios measured from these emission lines will allow us to probe shocks, constrain ionization parameters, and reveal the ionizing spectra, all of which would provide a clearer picture of the true nature of these galaxies.

All in all, expanding the sample of spatially resolved studies at high redshift will be crucial for building a more complete picture of the ISM conditions and feedback processes driving galaxy evolution during cosmic noon. Observation with JWST's NIRSpec IFU enables high S/N detections of faint rest-UV and optical emission lines at high spatial resolution, which provides more detailed mapping of ionization and chemical properties in the ISM. Meanwhile, ALMA observations of emission lines like [C II] in the far-IR can probe neutral gas and enable multi-phase analyses of the ISM. A broader, multi-wavelength approach incorporating these datasets will be essential for disentangling the interplay between star formation, feedback, and chemical enrichment in the early universe.

7. ACKNOWLEDGMENTS

We acknowledge support from NSF AAG grants AST-2009313 and AST-2307622. We also wish to extend special thanks to those of Hawaiian ancestry on whose sacred mountain we are privileged to be guests. Without their generous hospitality, the work presented herein would not have been possible.

REFERENCES

Abazajian, K. N., Adelman-McCarthy, J. K., Agüeros, M. A., et al. 2009, ApJS, 182, 543, doi: 10.1088/0067-0049/182/2/543

Acharyya, A., Krumholz, M. R., Federrath, C., et al. 2020, MNRAS, 495, 3819, doi: 10.1093/mnras/staa1100

Baldwin, J. A., Phillips, M. M., & Terlevich, R. 1981, PASP, 93, 5, doi: 10.1086/130766

Bian, F., Kewley, L. J., & Dopita, M. A. 2018, The Astrophysical Journal, 859, 175, doi: 10.3847/1538-4357/aabd74

Bian, F., Kewley, L. J., Groves, B., & Dopita, M. A. 2020, MNRAS, 493, 580, doi: 10.1093/mnras/staa259

Cappellari, M., & Copin, Y. 2003, MNRAS, 342, 345, doi: 10.1046/j.1365-8711.2003.06541.x

Carniani, S., Hainline, K., D'Eugenio, F., et al. 2024, Nature, 633, 318, doi: 10.1038/s41586-024-07860-9

Coil, A. L., Aird, J., Reddy, N., et al. 2015, ApJ, 801, 35, doi: 10.1088/0004-637X/801/1/35

Cullen, F., Shapley, A. E., McLure, R. J., et al. 2021, MNRAS, 505, 903, doi: 10.1093/mnras/stab1340

Curti, M., Maiolino, R., Cirasuolo, M., et al. 2020, MNRAS, 492, 821, doi: 10.1093/mnras/stz3379

Förster Schreiber, N. M., Renzini, A., Mancini, C., et al. 2018, ApJS, 238, 21, doi: 10.3847/1538-4365/aadd49

Förster Schreiber, N. M., Übler, H., Davies, R. L., et al. 2019, ApJ, 875, 21, doi: 10.3847/1538-4357/ab0ca2

Garcia, A. M., Torrey, P., Bhagwat, A., et al. 2025, arXiv e-prints, arXiv:2503.03804, doi: 10.48550/arXiv.2503.03804

Gibson, B. K., Pilkington, K., Brook, C. B., Stinson, G. S., & Bailin, J. 2013, A&A, 554, A47, doi: 10.1051/0004-6361/201321239

Hemler, Z. S., Torrey, P., Qi, J., et al. 2021, MNRAS, 506, 3024, doi: 10.1093/mnras/stab1803

Jones, G. C., Bunker, A. J., Telikova, K., et al. 2024, arXiv e-prints, arXiv:2405.12955, doi: 10.48550/arXiv.2405.12955

Jones, T., Ellis, R., Jullo, E., & Richard, J. 2010, ApJL, 725, L176, doi: 10.1088/2041-8205/725/2/L176

Jones, T., Ellis, R. S., Richard, J., & Jullo, E. 2013, ApJ, 765, 48, doi: 10.1088/0004-637X/765/1/48

Ju, M., Wang, X., Jones, T., et al. 2025, ApJL, 978, L39, doi: 10.3847/2041-8213/ada150

Kashino, D., Silverman, J. D., Sanders, D., et al. 2017, ApJ, 835, 88, doi: 10.3847/1538-4357/835/1/88

Kass, R. E., & Raftery, A. E. 1995, Journal of the American Statistical Association, 90, 773, doi: 10.1080/01621459.1995.10476572

Kauffmann, G., Heckman, T. M., Tremonti, C., et al. 2003, MNRAS, 346, 1055, doi: 10.1111/j.1365-2966.2003.07154.x

Kelly, B. C. 2007, ApJ, 665, 1489, doi: 10.1086/519947

Kewley, L. J., Dopita, M. A., Sutherland, R. S., Heisler, C. A., & Trevena, J. 2001, ApJ, 556, 121, doi: 10.1086/321545

Kriek, M., Shapley, A. E., Reddy, N. A., et al. 2015, The Astrophysical Journal Supplement Series, 218, 15, doi: 10.1088/0067-0049/218/2/15

Larkin, J., Barczys, M., Krabbe, A., et al. 2006, in Society of Photo-Optical Instrumentation Engineers (SPIE) Conference Series, Vol. 6269, Ground-based and Airborne Instrumentation for Astronomy, ed. I. S. McLean & M. Iye, 62691A, doi: 10.1117/12.672061

Leung, G. C. K., Coil, A. L., Azadi, M., et al. 2017, ApJ, 849, 48, doi: 10.3847/1538-4357/aa9024

Li, Z., Wang, X., Cai, Z., et al. 2022, ApJL, 929, L8, doi: 10.3847/2041-8213/ac626f

Lockhart, K. E., Do, T., Larkin, J. E., et al. 2019, AJ, 157, 75, doi: 10.3847/1538-3881/aaf64e

Lyke, J., Do, T., Boehle, A., et al. 2017, OSIRIS Toolbox: OH-Suppressing InfraRed Imaging Spectrograph pipeline, Astrophysics Source Code Library, record ascl:1710.021

Ma, X., Hopkins, P. F., Feldmann, R., et al. 2017, MNRAS, 466, 4780, doi: 10.1093/mnras/stx034

Madau, P., & Dickinson, M. 2014, ARA&A, 52, 415, doi: 10.1146/annurev-astro-081811-125615

Masters, D., McCarthy, P., Siana, B., et al. 2014, ApJ, 785, 153, doi: 10.1088/0004-637X/785/2/153

Momcheva, I. G., Brammer, G. B., van Dokkum, P. G., et al. 2016, ApJS, 225, 27, doi: 10.3847/0067-0049/225/2/27

Napolitano, L., Castellano, M., Pentericci, L., et al. 2025, A&A, 693, A50, doi: 10.1051/0004-6361/202452090

Parlanti, E., Carniani, S., Venturi, G., et al. 2025, A&A, 695, A6, doi: 10.1051/0004-6361/202451692

Runco, J. N., Shapley, A. E., Sanders, R. L., et al. 2021, MNRAS, 502, 2600, doi: 10.1093/mnras/stab119

Rupke, D. S. N., Kewley, L. J., & Chien, L. H. 2010, ApJ, 723, 1255, doi: 10.1088/0004-637X/723/2/1255

Sanders, R. L., Shapley, A. E., Clarke, L., et al. 2023, The Astrophysical Journal, 943, 75, doi: 10.3847/1538-4357/aca9cc

Scholtz, J., Maiolino, R., D'Eugenio, F., et al. 2023, arXiv e-prints, arXiv:2311.18731, doi: 10.48550/arXiv.2311.18731

Shapley, A. E., Reddy, N. A., Kriek, M., et al. 2015, The Astrophysical Journal, 801, 88, doi: 10.1088/0004-637X/801/2/88

Shapley, A. E., Sanders, R. L., Topping, M. W., et al. 2025, ApJ, 980, 242, doi: 10.3847/1538-4357/adad68

Steidel, C. C., Strom, A. L., Pettini, M., et al. 2016, ApJ, 826, 159, doi: 10.3847/0004-637X/826/2/159

Steidel, C. C., Rudie, G. C., Strom, A. L., et al. 2014, ApJ, 795, 165, doi: 10.1088/0004-637X/795/2/165

Strom, A. L., Steidel, C. C., Rudie, G. C., et al. 2017, ApJ, 836, 164, doi: 10.3847/1538-4357/836/2/164

Sánchez, S. F., Rosales-Ortega, F. F., Iglesias-Páramo, J., et al. 2014, A&A, 563, A49, doi: 10.1051/0004-6361/201322343

Tacconi, L. J., Genzel, R., & Sternberg, A. 2020, ARA&A, 58, 157, doi: 10.1146/annurev-astro-082812-141034

Tissera, P. B., Rosas-Guevara, Y., Bower, R. G., et al. 2019, MNRAS, 482, 2208, doi: 10.1093/mnras/sty2817

Topping, M. W., Shapley, A. E., Reddy, N. A., et al. 2020, MNRAS, 495, 4430, doi: 10.1093/mnras/staa1410

Übler, H., D'Eugenio, F., Perna, M., et al. 2024, MNRAS, 533, 4287, doi: 10.1093/mnras/stae1993

Wang, X., Jones, T. A., Treu, T., et al. 2019, ApJ, 882, 94, doi: 10.3847/1538-4357/ab3861

—. 2020, ApJ, 900, 183, doi: 10.3847/1538-4357/abacce

Weldon, A., Reddy, N. A., Topping, M. W., et al. 2022, MNRAS, 515, 841, doi: 10.1093/mnras/stac1822

—. 2023, MNRAS, 523, 5624, doi: 10.1093/mnras/stad1615

Wright, S. A., Larkin, J. E., Graham, J. R., & Ma, C.-P. 2010, ApJ, 711, 1291, doi: 10.1088/0004-637X/711/2/1291

Yuan, T. T., Kewley, L. J., & Rich, J. 2013, ApJ, 767, 106, doi: 10.1088/0004-637X/767/2/106

APPENDIX

A. SPECTRA AND FITTED PROFILES

A.1. *MOSFIRE and OSIRIS integrated spectra*

In this section of the appendix, we compare the Keck/MOSFIRE and Keck/OSIRIS integrated spectra for our sample, as seen in Fig. 12. These OSIRIS spectra have been corrected for the offset as determined by the OH line centroiding routine described in Section 2.2, but retain the systemic redshift determined from the MOSDEF survey. As discussed in Section 2.2, there is an offset in wavelengths between OSIRIS and MOSFIRE measurements, particularly for COSMOS 19985 and COSMOS 20062 where their OSIRIS spectra appear blueshifted with respect to those of MOSFIRE. Here, the integrated OSIRIS spectra, generated by summing spaxels within the 3 spatial-σ elliptical mask (or within the three clump bins in GOODS-S 40768), are normalized to the MOSFIRE spectra using the peak flux values of [O III]λ5008 in the H band and Hα in the K band.

All four galaxies prefer a two-component model fit, where the blue dashed line corresponds to the narrow component, and the orange line represents the broad component. Locations of strong emission lines are overlaid as light-gray vertical dotted-lines for reference.

Fig. 13 and 14 display the OSIRIS integrated spectra and MOSFIRE spectra respectively. Each panel shows the observed spectrum (black curve) along with the error spectrum (gray shaded region). The total fit is shown in green, with the linear continuum fit overlaid in red. Locations of key emission lines are indicated with vertical light-gray dotted lines for reference.

For the MOSFIRE spectra alone, all four galaxies prefer a two-component model fit. However, due to the limited S/N of the OSIRIS integrated spectra, only COSMOS 19985 prefers the two-component model as seen in Fig. 13. To ensure consistency in comparisons between the MOSFIRE and OSIRIS integrated spectra, the final fitted line profile of the MOSFIRE spectra are set to adopt the preferred component model (i.e. one- or two-components) of the corresponding OSIRIS integrated spectra.

While a one-component model fit is passable for the MOSFIRE spectra of AEGIS 3668 and GOODS-S 40768, we draw attention to the fact that such a model does not encapsulate the flux of COSMOS 20062 well, especially for Hα in the K band (Fig. 13). A detailed comparison of more complex models is presented in Appendix Section B.

A.2. *Radial and clump bins*

In Figs. 15–18, we showcase the emission line fitting for the radial and clump bins as defined in Section 3.1.1. The color scheme follows that of Fig. 13. In each row, the upper-left red text box contains the bin name and whether a one-component model (1) or two-component model (2) is preferred and plotted. A "refitted" tag is displayed at the top right of the band that underwent refitting as determined by the routine described in Section 3.2.1. In Figs. 16 and 18, the circular clump bins are shown.

A.3. *Voronoi bins*

In Figs. 19–21, we showcase the emission line fitting for the Voronoi bins as defined in Section 3.1.2. The color scheme follows that of Fig. 13. The upper-left corner of each panel shows the bin name and whether a one-component model (1) or two-component model (2) is preferred and plotted.

B. BIC COMPARISONS

As mentioned in Appendix Section A.1, Fig. 22 displays spectral fits for the OSIRIS integrated spectrum of COSMOS 20062, comparing different models to assess the best-fit solution. The original one-component model, determined by the fitting routine in Section3.2.1, is shown alongside alternative models incorporating an additional broad Hα component in one- and two-component profiles, as well as a three-component model. The BIC values for each fit are displayed in the upper-right corner of each panel, with the best-fit model determined by the lowest BIC value. Despite the significant residuals, the analysis finds that the original one-component model remains the preferred fit.

Similarly, Fig. 23 highlights Voronoi bins in COSMOS 19985 where the initial model does not yield the lowest BIC value. Among the four bins examined, only Bin 0 (the central-most spaxel) exhibits a reduction of ΔBIC > 6, favoring a more complex model with a narrow and broad [N II]$\lambda\lambda 6548, 6585$+H$\alpha$ component and a broad Hα component.

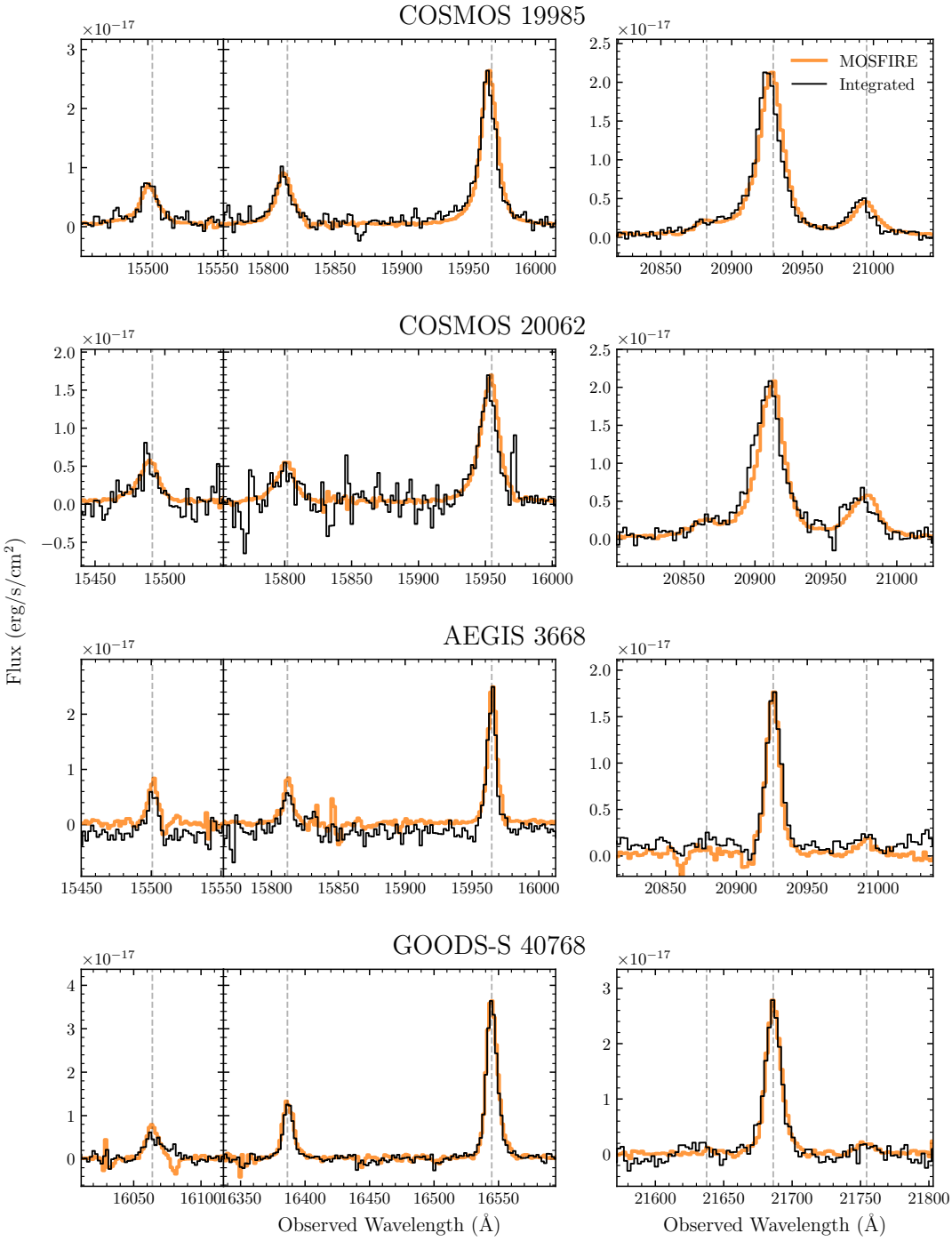

Figure 12. OSIRIS and MOSFIRE integrated spectra. The left column shows Hβ and [O III]$\lambda\lambda$4960, 5008 from the H band, while the right column shows [N II]$\lambda\lambda$6548, 6585 and Hα from the K band. The integrated spectra (black curves) are generated by summing the spectra in the spaxels within the 3 spatial-σ elliptical galaxy mask for COSMOS 19985, COSMOS 20062, and AEGIS 3668 and the spaxels within the three clump bins in GOODS-S 40768. The orange overlaid curves are the spectra taken by Keck/MOSFIRE. The OSIRIS spectra were normalized to those from MOSFIRE by matching the peak flux values of [O III]λ5008 for the H band and Hα for the K band.

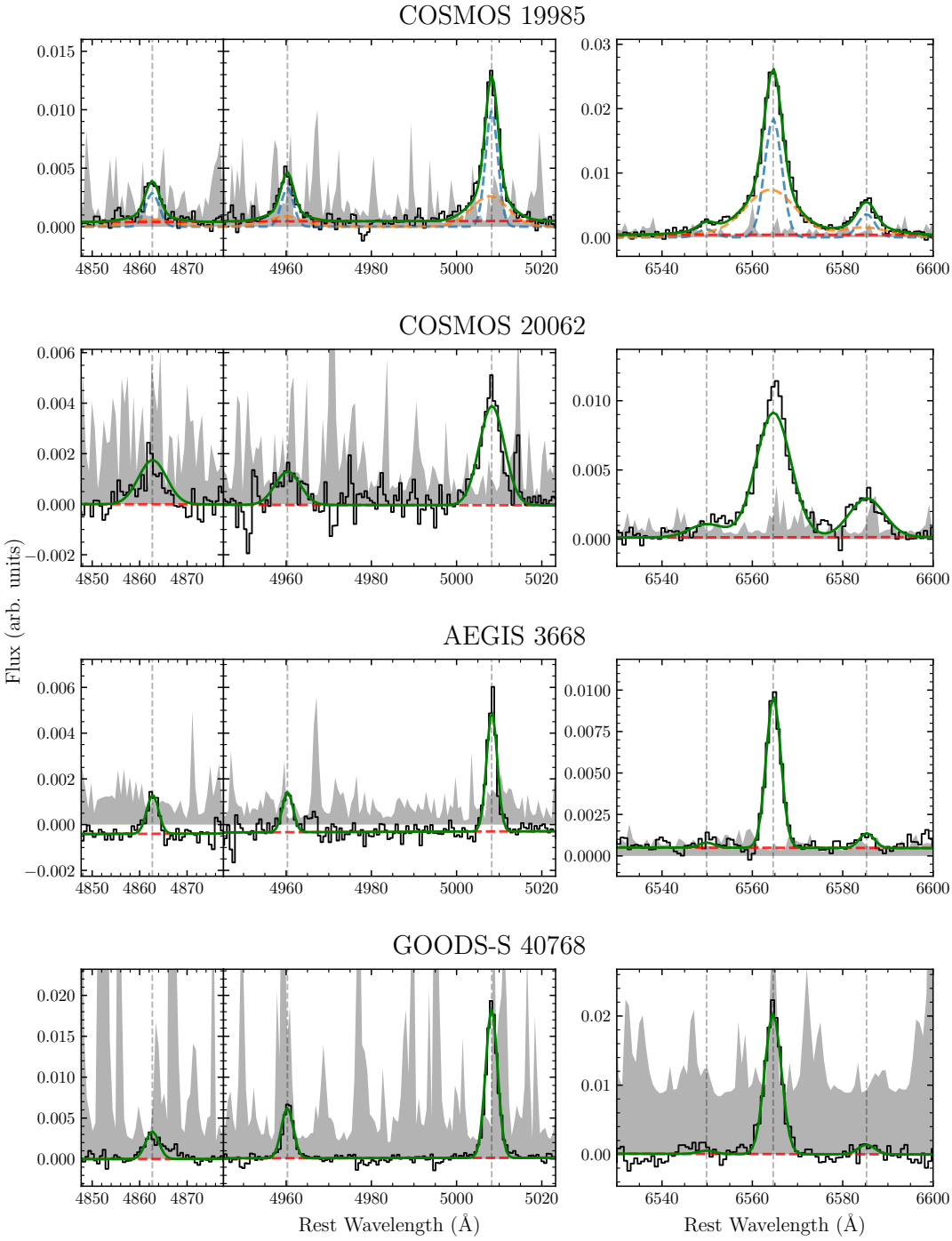

Figure 13. OSIRIS integrated spectra and fitted profiles. The black curves and gray shaded regions represent the flux and error spectra. The green solid curve represents the total fit, while the red dashed line shows the linear continuum fit around the emission lines. For COSMOS 19985, which prefers a two-component model fit, the blue dashed line corresponds to the narrow component, and the orange line represents the broad component. Locations of strong emission lines are overlaid as light-gray vertical dotted-lines for reference.

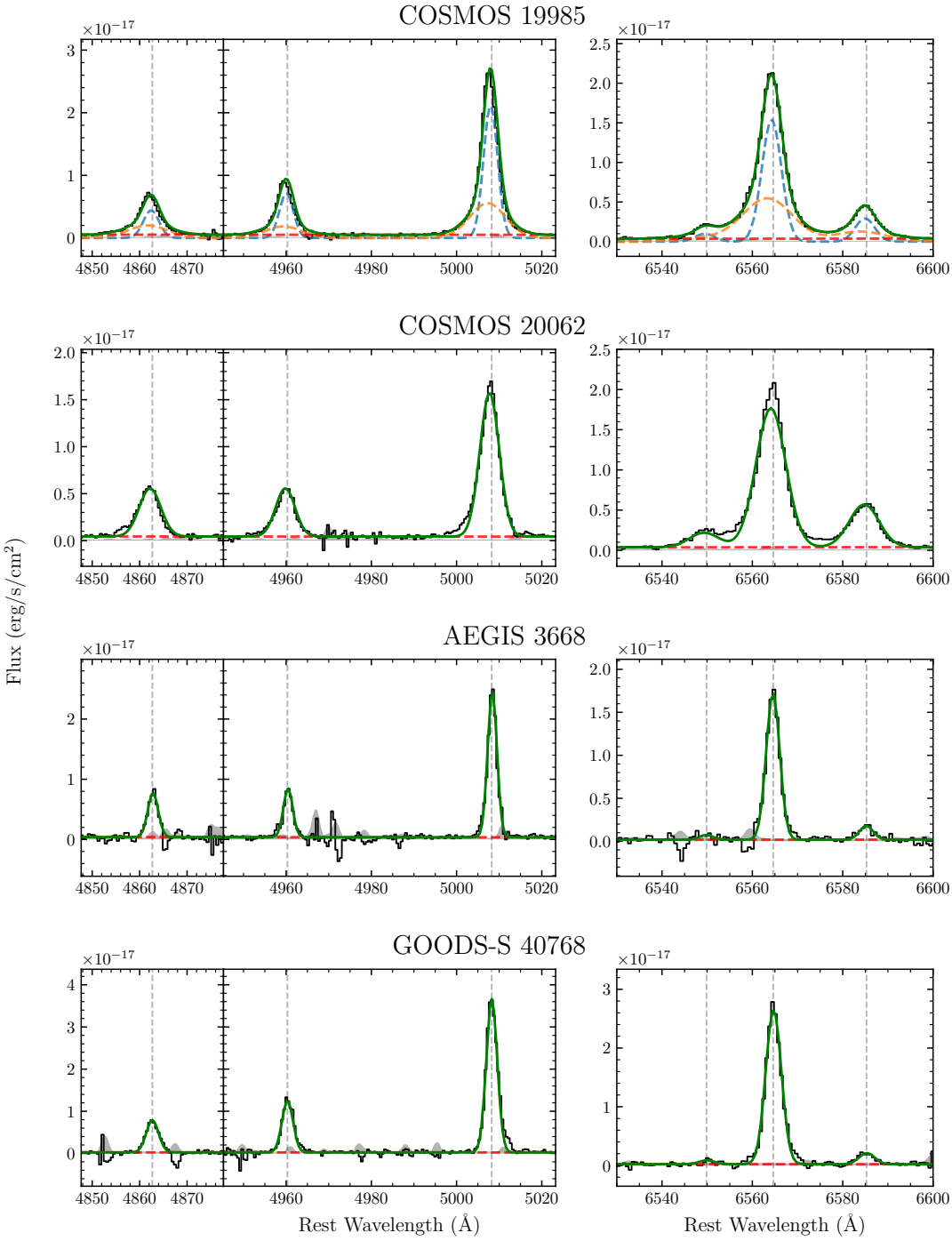

Figure 14. MOSFIRE spectra and fitted profiles. The left column shows Hβ and [O III]$\lambda\lambda$4960, 5008 from the H band, while the right column shows [N II]$\lambda\lambda$6548, 6585 and Hα from the K band. The black curves and gray shaded regions represent the flux and error spectra. The green solid curve represents the total fit, while the red dashed line shows the linear continuum fit around the emission lines. COSMOS 19985 is fit with a two-component model, while the other three galaxies are fit with a one-component model according to the preference of the integrated OSIRIS spectra in Fig. 13. For the two-component model fit in COSMOS 19985, the blue dashed line corresponds to the narrow component, and the orange line represents the broad component. Locations of strong emission lines are overlaid as light-gray vertical dotted-lines for reference.

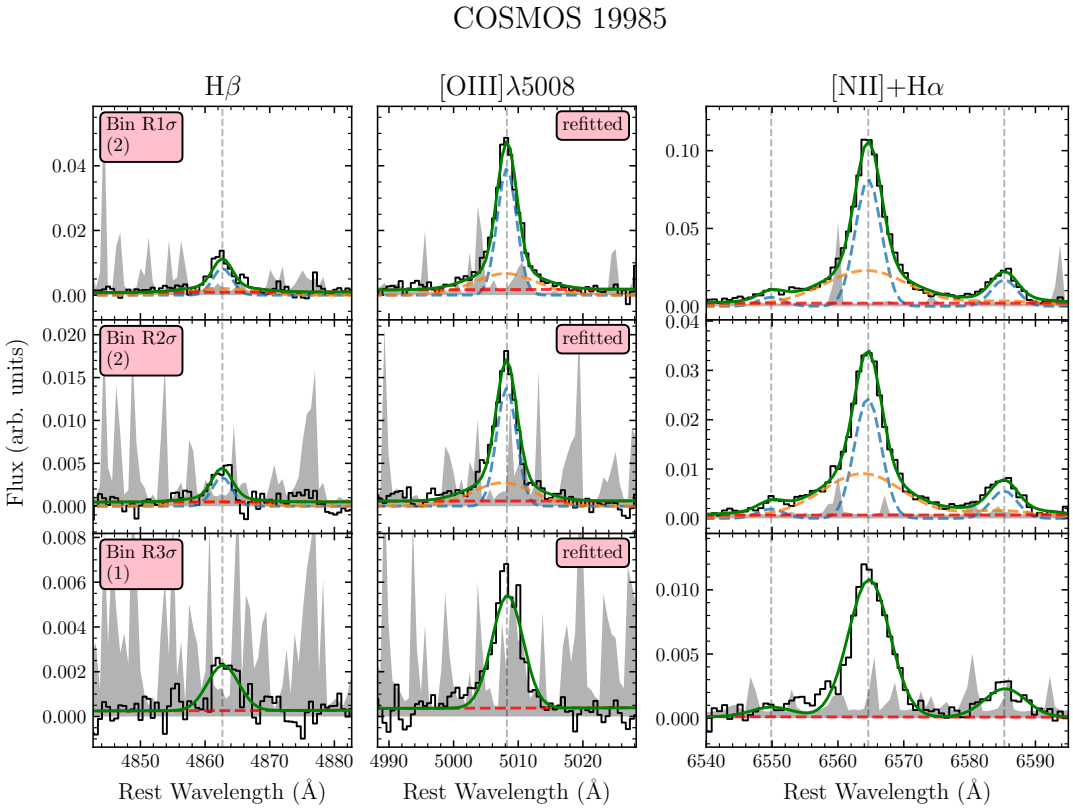

Figure 15. Radially-binned spectra for COSMOS 19985 and fitted line profiles. The left column shows Hβ and [O III]λ5008 from the H band and the right column shows the [N II]$\lambda\lambda$6548, 6585+Hα group from the K band. The color scheme follows that of Fig. 13. The red text box contains the bin name and whether a one-component model (1) or two-component model (2) is preferred and plotted. A "refitted" tag is displayed at the top right of the band that underwent refitting as determined by the routine described in Section 3.2.1.

COSMOS 20062

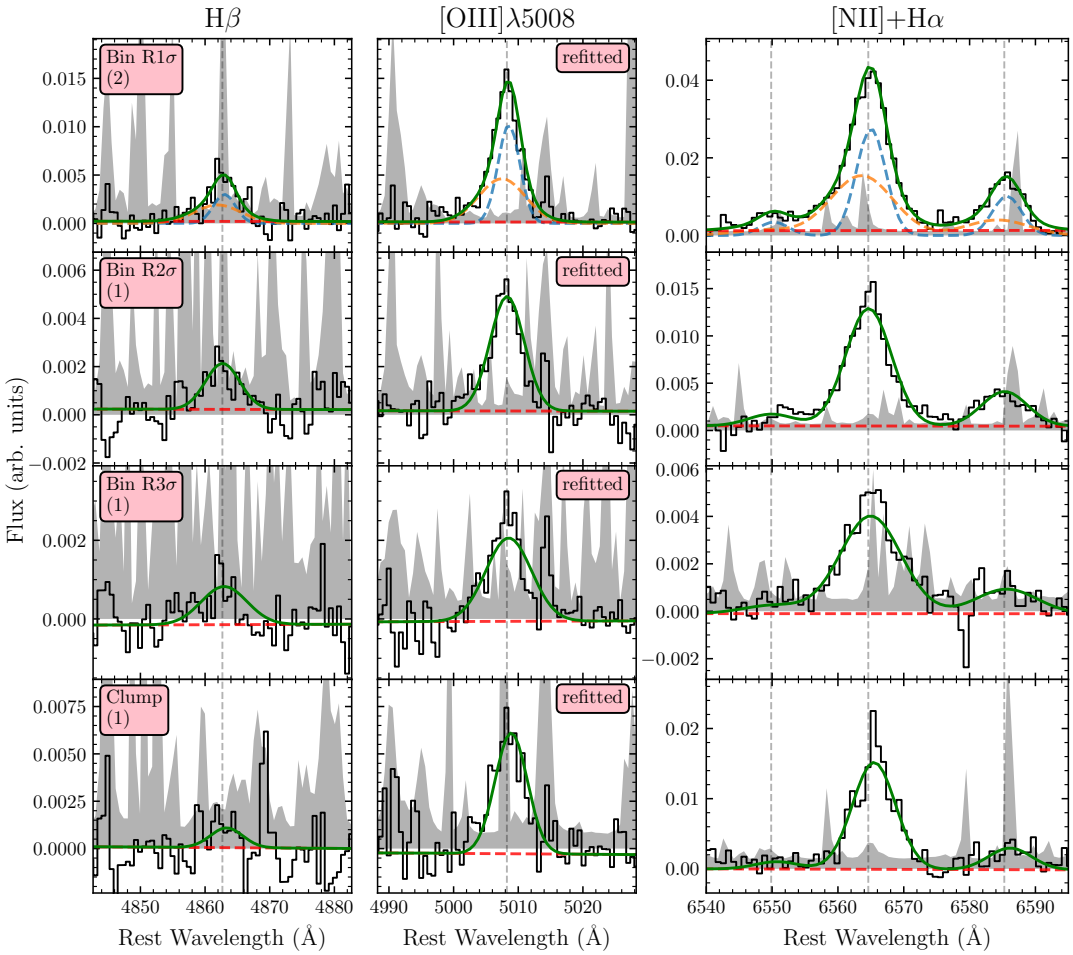

Figure 16. Radially-binned spectra for COSMOS 20062 and fitted line profiles, similar to Fig. 15. The last row shows the clump bin shown in Fig. 2.

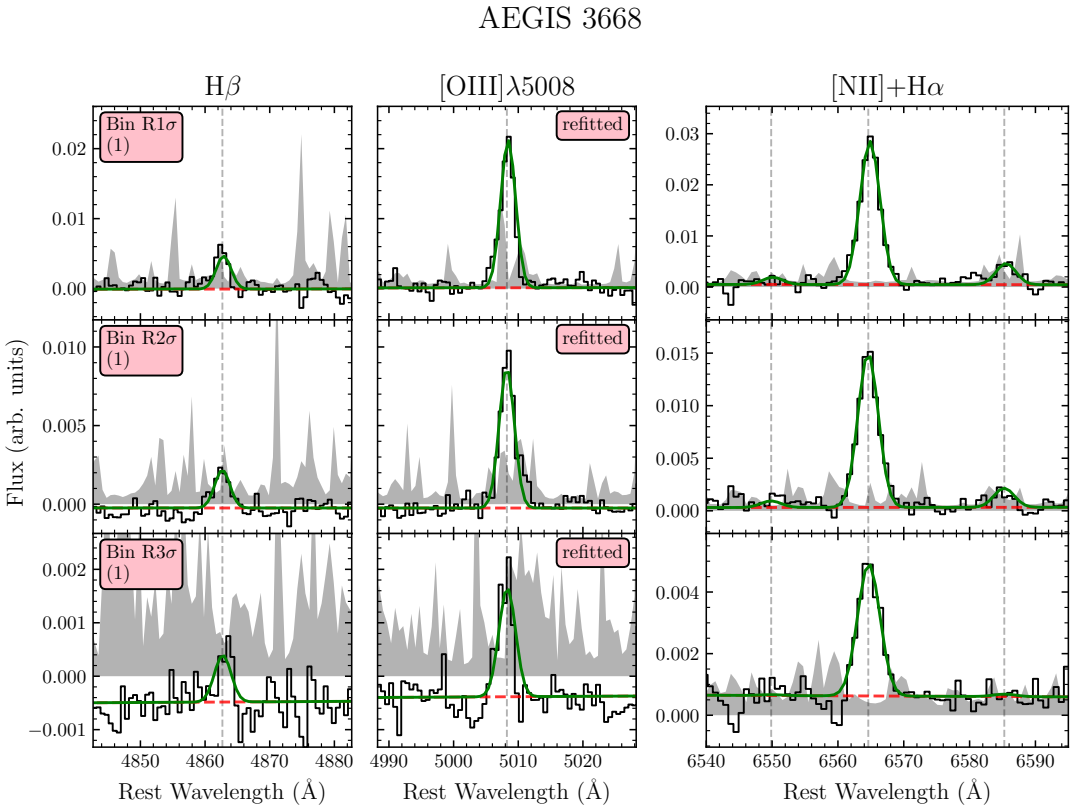

Figure 17. Radially-binned spectra for AEGIS 3668 and fitted line profiles, similar to Fig. 15.

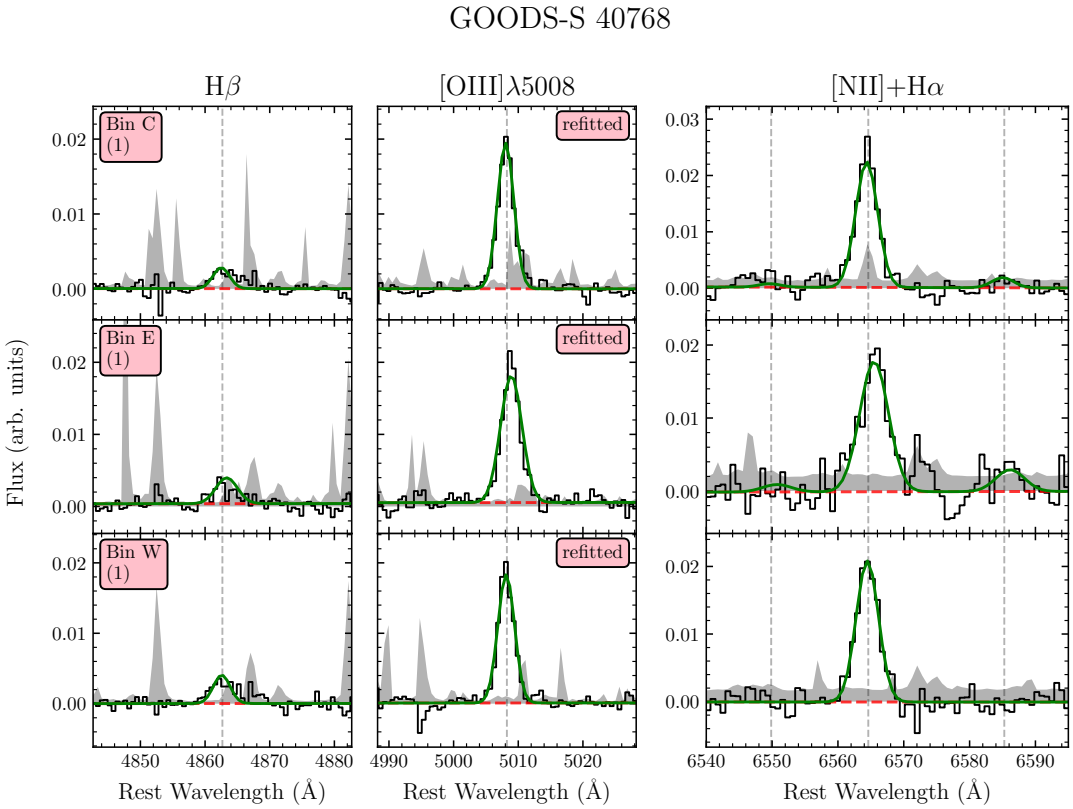

Figure 18. Clump-binned spectra for GOODS-S 40768 and fitted line profiles, similar to Fig. 15.

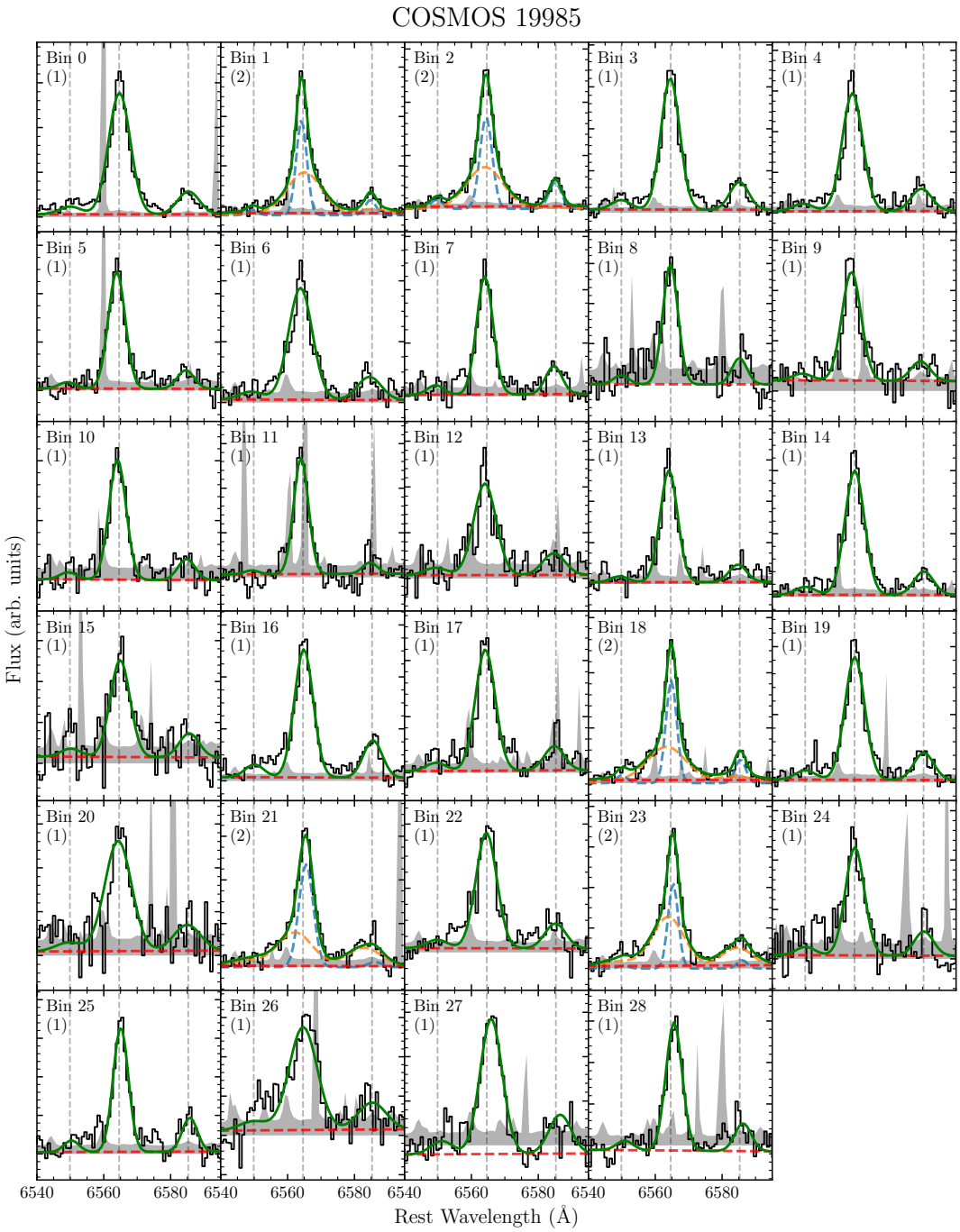

Figure 19. Voronoi-binned K-band spectra for COSMOS 19985 and fitted line profiles. The color scheme follows that of Fig. 13. The upper-left corner of each panel displays the bin name and whether a one-component model (1) or two-component model (2) is preferred and plotted.

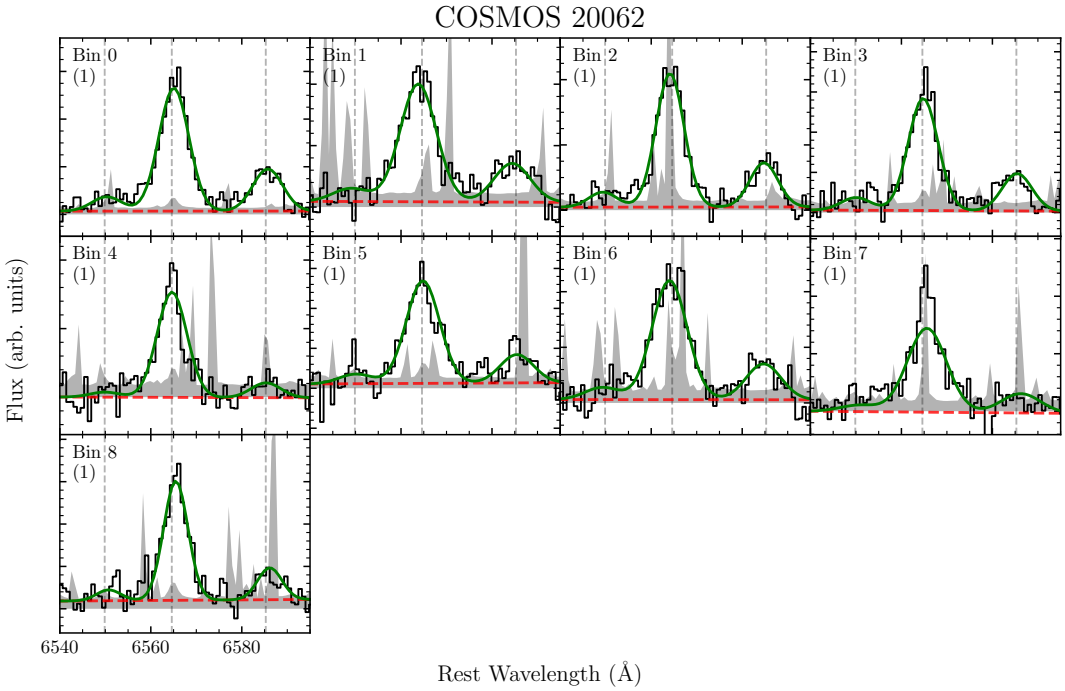

Figure 20. Voronoi-binned K-band spectra for COSMOS 20062 and fitted line profiles, similar to Fig. 15.

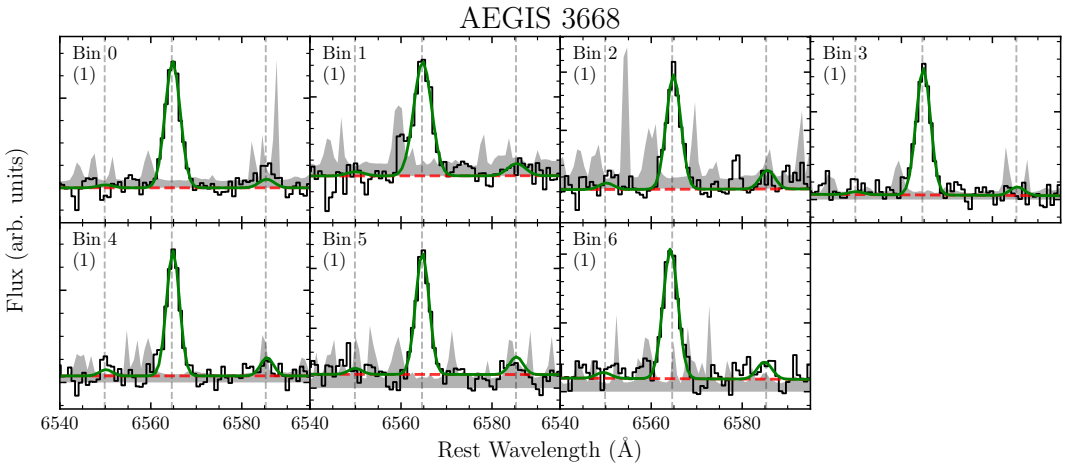

Figure 21. Voronoi-binned K-band spectra for AEGIS 3668 and fitted line profiles, similar to Fig. 15.

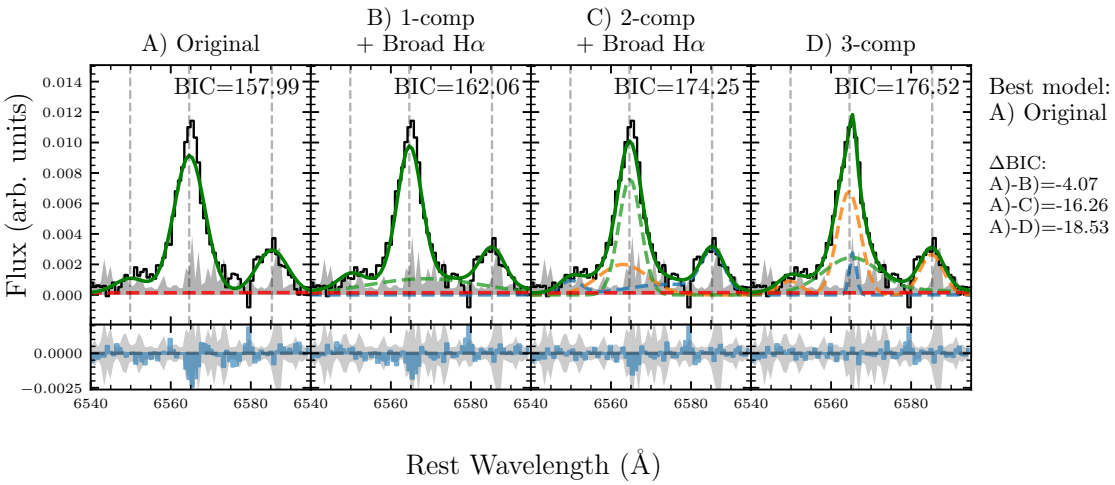

Figure 22. Spectral fits for the OSIRIS integrated spectrum of COSMOS 20062. The color scheme follows that of Fig. 13. The BIC value of each fit is quoted at the upper-right corner of each panel. Model A) is the one-component model preferred by the routine described in Section 3.2.1. Models B) and C) are one- and two-component profiles with an additional broad Hα Gaussian. Model D) is a three-component model. The best model, as determined by BIC analysis, is shown in the right column, along with the differences in BIC values between models. Despite the large residuals, the original one-component model is preferred.

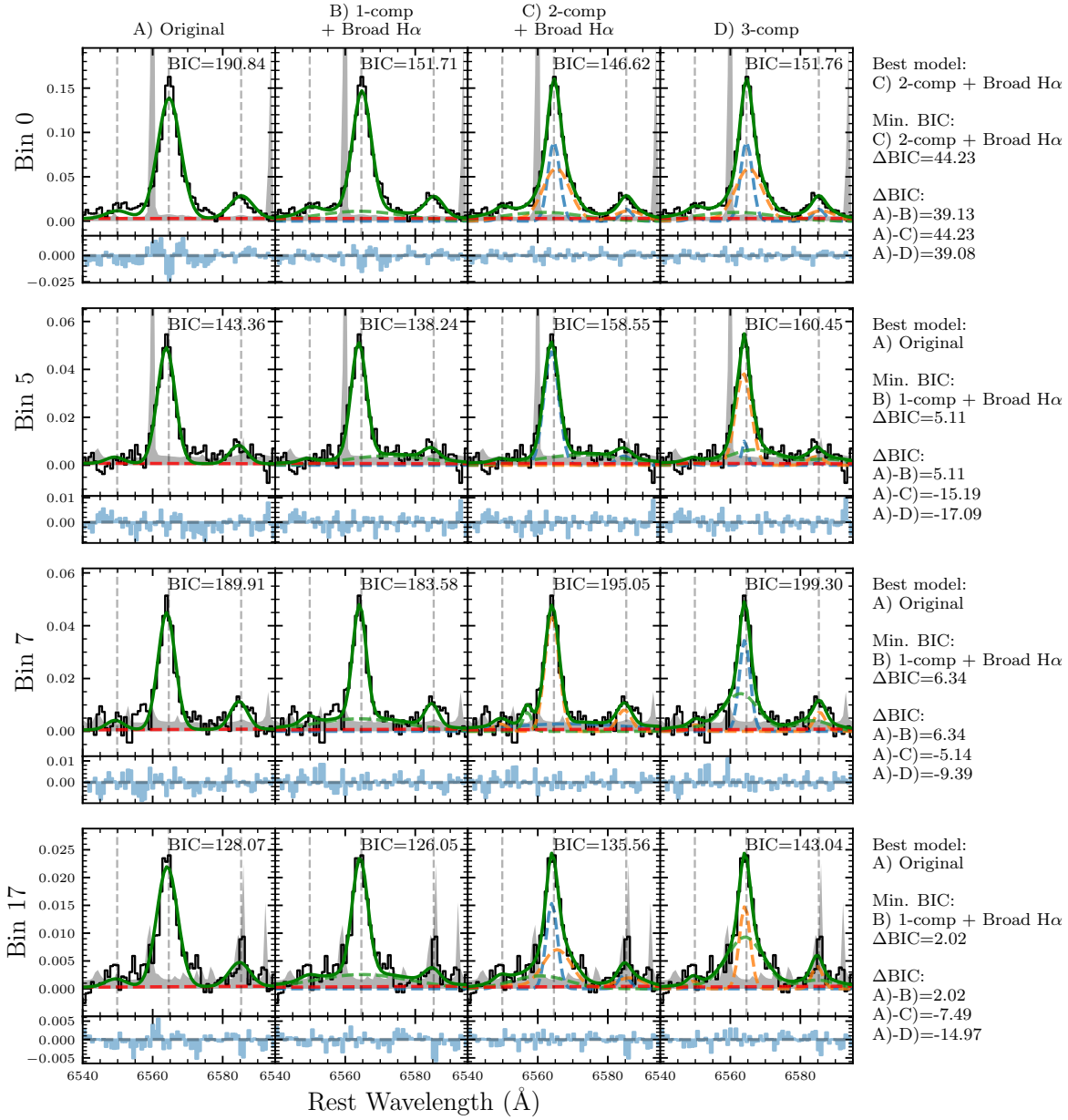

Figure 23. Spectral fits for a sample of Voronoi bins in COSMOS 19985 where the original fit does not have the lowest BIC value. The plotting scheme is similar to that of Fig. 22. Of the four bins shown, only Bin 0 has a reduction of ΔBIC > 6 as compared to the original model to favor the more complex model.